DISCLAIMER

Demonstration of the surveillance test article for an advanced reactor surveillance test program

INL/RPT-25-87662
Revision 0

Advanced Materials and Manufacturing Program

SEPTEMBER 2025

Heramb Mahajan,
Xinchang Zhang,
Ruchi Gakhar,
Kuo Yuan, and
Michael McMurtrey

Idaho National Laboratory

Idaho National Laboratory

Battelle Energy Alliance manages INL for the U.S. Department of Energy's Office of Nuclear Energy

INL/RPT-25-87662
Revision 0

Demonstration of the surveillance test article for an advanced reactor surveillance test program

Heramb Mahajan,
Xinchang Zhang,
Ruchi Gakhar,
Kuo Yuan, and
Michael McMurtrey
Idaho National Laboratory

SEPTEMBER 2025

Idaho National Laboratory
Idaho Falls, Idaho 83415

http://www.inl.gov

Prepared for the
U.S. Department of Energy
Office of Nuclear Energy
Under DOE Idaho Operations Office
Contract DE-AC07-05ID14517

Page intentionally left blank

SUMMARY

Operational environments in generation IV reactors involve corrosive and irradiative conditions at elevated temperatures. Typical reactor operations consist of transients that impose cyclic loads on reactor components, in addition to creep damage occurring during normal operation. These cyclic loads and creep damage, combined with corrosive and irradiative environments, result in synergistic degradation of component materials. However, limited data exists on the coupled damage effects on materials for reactor environments. While the surrogate material surveillance concept has been used in light water reactors to assess irradiation damage, existing material surveillance technologies are not suitable for in-situ monitoring of coupled material degradation expected for advanced reactors.

The materials surveillance program focuses on material degradation management and the estimation of remaining life of reactor components through surveillance test articles (STAs). This paper presents the design and analysis methodology of a bi-metal surveillance test article, which uses difference in thermal expansion coefficient between two metals to induce in-situ loads. This report presents the work conducted in Fiscal Year (FY) 2025, to test the STA in air and salt environments. These test specimens were evaluated after thermal cycle exposure and remaining life is measured through creep test.

Page intentionally left blank

ACKNOWLEDGMENTS

This research was sponsored by the U.S. Department of Energy (DOE) under Contract No. DE-AC07-05ID14517 with Idaho National Laboratory (INL), which is managed and operated by Battelle Energy Alliance. Programmatic direction was provided by the Office of Nuclear Research Deployment of the DOE Office of Nuclear Energy (NE).

The authors gratefully acknowledge the support provided by Sue Lesica of DOE-NE, who worked as a federal lead for Advanced Materials, Advanced Reactor Technologies (ART) Program, Janelle Eddins of DOE-NE, federal manager, ART Molten Salt Reactors (MSR) Campaign, and Patricia Paviet of Pacific Northwest National Laboratory, national technical director, ART MSR Campaign. Authors also acknowledge support provided by Li Meimei, National Technical Director of Advanced Materials and Manufacturing (AMMT).

The authors also thank Qiufeng Yang, David Cottle, Austin Matthews, Tate Patterson, Alex Pomo, and Asa Monson from INL for experimental support.

Page intentionally left blank

CONTENTS

CONTENTS

FIGURES

TABLES

Page intentionally left blank

ACRONYMS

ANL	Argonne National Laboratory
ASME	American Society of Mechanical Engineers
ASTM	American Society of Testing and Materials
BN	Boron Nitride
BPVC	Boiler and Pressure Vessel Code
CTE	Coefficient of Thermal Expansion
DED	Directed Energy Deposition
DIC	Digital Image Correlation
DOE	(US) Department of Energy
EDS	Energy Dispersive Spectroscopy
FRP	Fast Reactor Program
FY	Fiscal Year
HTR	High-Temperature Reactors
INL	Idaho National Laboratory
LVDT	Linear Variable Differential Transformer
NE	(Office of) Nuclear Energy
SEM	Scanning Electron Microscope
SPCT	Small Punch Creep Test
SPT	Small Punch Test
STA	Surveillance Test Article
XCT	X-ray Computed Tomography

Page intentionally left blank

Demonstration of the surveillance test article for an advanced reactor surveillance test program

1. INTRODUCTION

Generation IV nuclear reactors have an operating temperature range from 500–900°C. Some of these high-temperature reactor (HTR) designs have corrosive fluid coolants, such as molten salts, with a typical operation temperature range of 500–700°C. Materials used for HTR component construction are subjected to elevated temperature transients and corrosive environments in the presence of irradiation. The American Society of Mechanical Engineers (ASME) Boiler and Pressure Vessel Code, Section III, Division 5, provides the component construction rules (ASME 2025). These rules support the mechanical design of components; however, Section III Division 5 code does not specify the design rules for degradation of metallic materials due to corrosion and irradiation. Very limited information is available on synergistic material degradation due to corrosion, erosion, and creep-fatigue mechanical damage. Developing a large material database for each HTR coolant design, a variety of materials, and up to 60 years of design life is not practical. Thus, material degradation under HTR environments poses a challenge for long-term design.

The material surveillance program collects in-situ material degradation information from HTRs and uses that information to support the design and licensing of HTRs. This approach has been implemented with light water reactors to monitor irradiation damage on graphite and embrittlement of pressure vessel steel. A surveillance sample is placed in the reactor to accumulate the irradiation damage. This sample is periodically removed from the reactor and assessed for accumulated damage. This information is used to estimate the damage accumulation in the other parts of the reactor to determine the remaining life. Although the material surveillance program for HTRs is similar to the historic in-situ program for light water reactors, there is a key challenge. Typical reactor operations undergo power transients which results in temperature transients on components. These transients result in cyclic load at elevated temperatures that induces creep-fatigue damage in component materials at elevated temperatures. The challenge is to apply in-situ cyclic load. The American Society of Testing and Materials (ASTM) E531-2023 standard describes the practice for surveillance testing of high-temperature nuclear component materials (ASTM 2023). This ASTM standard does not provide information regarding how to induce in-situ cyclic loads. Thus, there is a gap in the material surveillance technology for HTRs to capture the mechanical damage due to cyclic loads at elevated temperatures.

A bi-metal configuration was proposed that uses the difference of expansion coefficients between two materials to induce cyclic loads, and further research work developed a cylindrical test article that successfully showed a proof-of-concept design (Messner et al. 2018). Acceptance criteria have been proposed to use test results and decide the acceptance of material based on remaining life assessment. To mitigate the large sample size, a new flat sample design was fabricated and tested under a variety of different temperature transients (McMurtrey et al. 2022, Mahajan et al. 2023 and Zhang et al. 2024).

This report presents the surveillance test article (STA) design and fabrication approach and test data from thermal cycling test articles in air and salt environments. The STA samples were subjected to temperature cycles inducing passively actuated cyclic load. The recorded strain data from Digital Image Correlation (DIC) are presented. The mechanical damage is calculated and compared against remaining life determined from the creep rupture test on the sample that has gone through temperature transients.

2. EXPERIMENT STRATEGY

The overview of experimental strategy is illustrated with three Cases. Case 1: STAs are subjected to thermal cycles in given environment till failure in the gauge length is observed. Case 2: Partial thermal cycles were applied on the test article in given environment such that the total damage fraction is less than one. Then the test article is removed from furnace, and test specimen is destructively tested to evaluate the remaining creep life. Case 3: A pure creep test on the test specimen is conducted as a benchmark creep life.

This report presents data from Case 2 and Case 3, where Case 2 discusses the testing in air, FLiNaK, and NaCl-MgCl2. This section presents an overview of test article design, experimental procedure and test setup for testing in air and in salt environments. Last subsection presents the post-test evaluation techniques, which consists of small punch test at elevated temperatures and pure creep test.

2.1. Overview of Test Article Design

Previous report discussed the STA design methodology (Mahajan et al. 2023). This section presents an overview of test article design for discussion purposes. The STA operates on the principle of difference in the bi-metal coefficient of thermal expansion (CTE). The CTE difference is used to apply a temperature-dependent cyclic load on materials. The STA consists of a specimen which is a material to be surveilled, a driver which has lower CTE compared to the specimen, and columns to induce thermal mismatch as shown in Figure 1. The STA design procedure involved a two-step approach. First, a three-bar model based simplified analysis developed by Argonne National Laboratory (ANL) was used to estimate the initial STA dimensions (Messner et al. 2022). This step assumes that specimens, driver, and columns act as a solid bar and neglects stress concentration due to notch geometries of specimen, drivers, and columns. This procedure uses the material model framework Nuclear Engineering Materials Library (NEML, 2023). A genetic algorithm optimization scheme available on the standard Python optimization library was used to determine the optimum STA dimensions. The second step involves a detailed finite element analysis which captures the local stresses near notch and welded regions. In this work, perfect contact was used to model bi-metal welds.

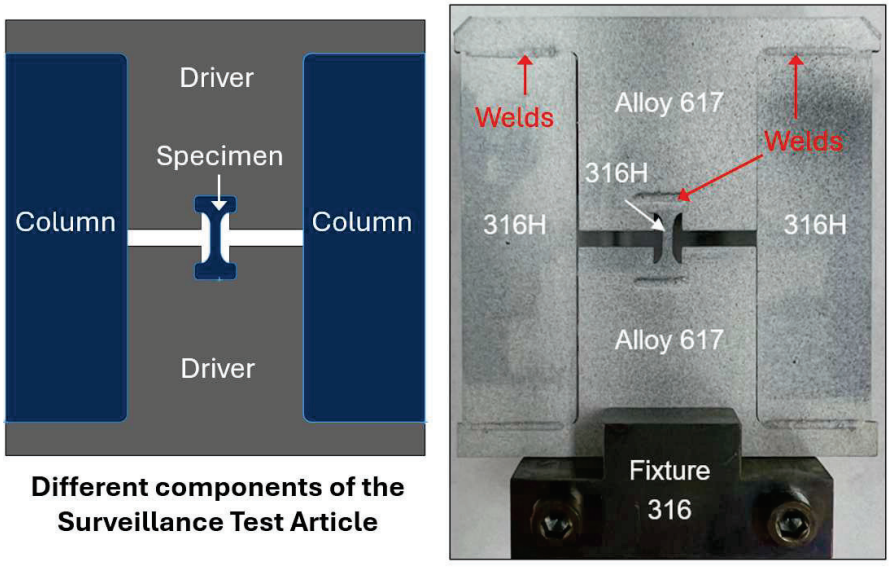

Figure 1. Schematic representation of the surveillance test article design showing specimen (SS 316H), drivers (Alloy 617), and columns (SS 316H).

Initial work conducted has established the proof-of-concept of the STA for cylindrical test articles. Although these studies were successful in capturing the target strain range and elastic follow-up, the large test article size was a drawback. Large STA could influence the fluid flow and thus interfere with the reactor operations. Activated volumes of large STA also pose a limitation on the application of surveillance technology. Hence, in this study flat test articles were designed and fabricated with reduced dimensions. The nominal width and height of the rectangular test article was 50 mm (~2 inch), and the thickness was 1.1 mm. Wire electro discharge machining was used to machine specimen, drivers, and columns. The columns and driver, and drivers and specimen, were welded with an e-beam welder and 316 filler powder as shown in Figure 1.

The surveillance specimens were fabricated in a composite configuration consisting of a central coupon of 316H stainless steel embedded within an Alloy 617 frame, with overall dimensions of 2”x2”. This configuration enabled direct comparison of the corrosion behavior of the two candidate structural materials under identical exposure conditions and reflected practical reactor environments in which dissimilar alloys are often in service together. A schematic of the specimen design is shown in Figure 4, highlighting the central 316H coupon and the surrounding Alloy 617 frame.

2.2. Surveillance Test Article Tests in Air

2.2.1. Experimental Setup

Cyclic thermal testing of STAs was performed using the furnace setup shown in Figure 2. The system consisted of a tube furnace for imposing temperature cycles, a DIC system for monitoring strain evolution, and a data acquisition unit for recording temperature profiles during the experiments. The experiments were conducted in air. The furnace was specially configured for high-temperature DIC measurements by addressing challenges that exist in measuring deformation at elevated temperatures using the DIC technique. These challenges include sample thermal radiation that can saturate images and obscure speckle patterns, degradation of speckle patterns due to prolonged exposure at elevated temperatures, and temperature gradients in the air that can induce refractive index variations and image distortions. To mitigate these effects, multiple strategies were implemented, including the use of a blue light source and a blue bandpass filter to suppress interference from specimen thermal radiation and enhance speckle contrast, the use of a quartz window mounted at the furnace end to limit air convection at the camera viewport and reduce heat-haze effect, and the use of a high-temperature-resistant speckle paint that can withstand temperatures up to ~1000°C. A Type K thermocouple was positioned adjacent to the test articles to record the local temperature during testing. Prior correlation between the furnace control temperature and specimen temperature was established. A more detailed description of the furnace setup and validation experiments is provided in our previous reports (Mahajan et al. 2023, and Zhang et al. 2024).

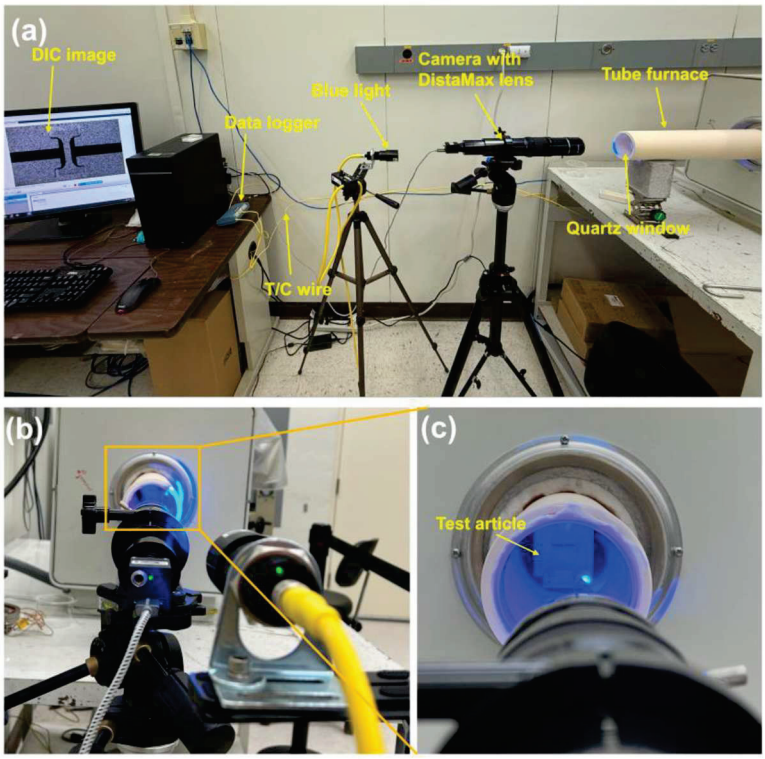

Figure 2. (a) Front view and (b) side view of the furnace testing setup with (c) a test article in cyclic thermal testing. The furnace testing consists of a DIC system to monitor strain evolution with a blue light source, a blue band-pass filter, and a quartz window to enhance imaging quality.

Cyclic temperature loading with a temperature dwell at peak temperatures was applied to the test articles to accumulate creep-fatigue damage. Since long-term cycling is required to generate measurable damage, testing with a single furnace setup limits efficiency and throughput. To address this, a parallel testing capability was developed as shown in Figure 3, building upon the procedures established in the tube furnace setup (Figure 2. This new configuration incorporates dual DIC systems, enabling simultaneous monitoring of two test articles. Parallel testing was achieved by positioning two test articles within the furnace, each aligned with a dedicated camera viewport for DIC imaging. The setup was validated through temperature calibration and strain measurement tests. For temperature calibration, a thermocouple was placed adjacent to a test article to measure furnace temperatures. The calibration showed the furnace temperature matched the controller readings within ±2°C at 700°C. A maximum cooling rate of 3.5°C/min was achieved, lower than the typical cooling rate (10°C/min) used in the tube furnace setup. To verify DIC performance, a test article was subjected to 10 thermal cycles between 500°C and 700°C, with a 30 min dwell at peak and valley temperatures. Both DIC systems measured a consistent strain range of 0.5% through absolute strain values differed. The discrepancy in absolute strain values was attributed to the out-of-plane bending of the specimen relative to the driver-column of the test article which produced residual tension on one side and compression on the other side of the specimen. Overall, the validation testing confirmed the readiness of the new furnace testing system for accelerated creep-fatigue testing.

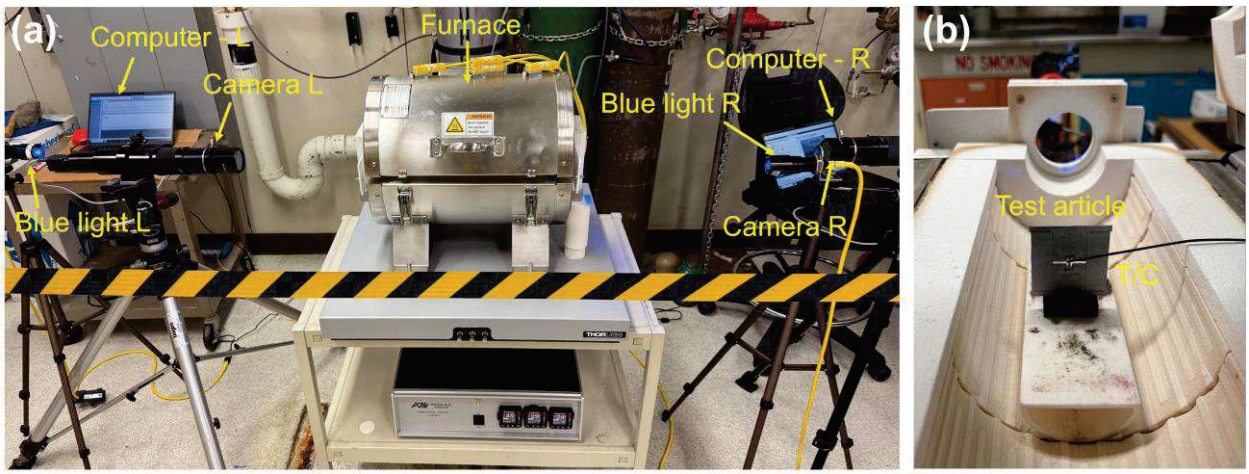

Figure 3. (a) A second furnace testing setup consisting of a dual DIC system with blue light to enable simultaneous testing of two test articles. (b) Furnace interior and placement of a test article and thermocouple in the furnace for system validation.

2.2.2. Digital Image Correlation

DIC was employed to track strain evolution of the test articles during cyclic thermal loading. As a non-contact optical measurement technique, DIC enables precise tracking of displacement and strain by correlating sequential images captured during deformation. The method relies on identifying and following fine surface features to compute local deformation and derive strain fields. Preparation of high-quality speckle patterns is therefore essential for reliable and high-fidelity strain measurement. Key requirements for effective speckle patterns include randomness and non-repetition, appropriate feature size relative to the specimen geometry and camera field-of-view, strong adhesion to ensure synchronized deformation, and thermal stability to maintain integrity at elevated temperatures. In this project, the miniature size of the 316H gauge section in the test articles necessitated the use of an airbrush technique to apply fine, random speckles. The procedure involved first applying a high-temperature white primer as a base layer, drying it overnight, and subsequently spraying black speckles using an airbrush to form the final pattern. Representative speckle patterns for two test article designs (Alloy 617-316H in Figure 4a and Alloy 244-316H in Figure 4b) are shown in Figure 4. The quality of the speckle patterns were evaluated using both an optical microscope and the DIC imaging system (FLIR Blackfly BFS-U3-27S5M camera with a DistaMax K2 lens). These examinations confirmed good contrast, fine spatial details, and strong adhesion of the speckles to the substrate. The speckle pattern preparation and strain comparison between DIC and extensometers were validated previously using elevated-temperature tensile and creep tests.

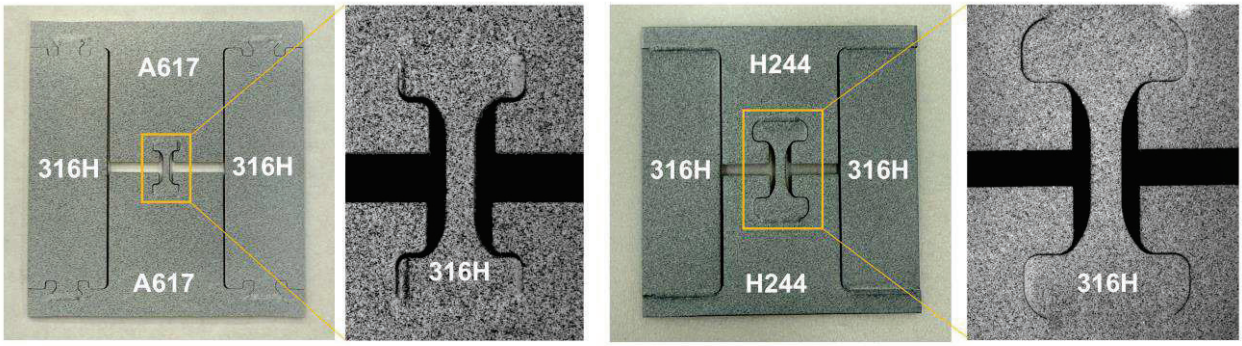

(a) (b)

Figure 4. Surveillance test article specimen design with DIC speckle patterns prepared on test articles with (a) Alloy 617 and (b) Alloy 244 as the driver material.

2.2.3. Surveillance Test Articles and Testing Load Cycles

Previous test-to-rupture cyclic testing on STAs revealed weld failure between Alloy 617 drivers and 316H specimens after a long-term cyclic testing (1012 cycles). Post-test X-ray computed tomography (XCT) analysis confirmed the presence of cracking and defects at the welds. The failed test articles were welded using directed energy deposition (DED) with SS 316 filler material. In FY25, the welding procedure was improved by optimizing welding parameters and replacing the SS 316 filler with Inconel 718 to enhance weld strength. Six test articles (WSTA 1-6) were fabricated using the improved parameters. All six test articles were scanned using XCT to examine the quality of welds. Figure 5 shows XCT images of two test articles, demonstrating defect-free welding. The weld penetration is about 33% through the specimen thickness, and no cracks or defects were identified.

Table 1 summarizes the furnace testing temperature profiles, which includes temperature cycling between 500°C and 700°C at 8°C/min heating and cooling rates and a 0.5 hr dwell at the peak temperature. Various temperature profiles were used previously to evaluate strain response under different thermal events, including changing valley temperatures and ramp rates. Previous testing results suggest that variations in heating and cooling rates have minimal impact on the strain response, demonstrating the robustness of the test article design for monitoring material degradation across different reactor temperature variance events.

In FY25, the six STAs were tested according to the design in Table 1. WSTA-1 was tested in air using the furnace setup (Figure 2). The objective was to apply sufficient thermal cycles to either induce specimen fracture or produce a significant reduction in strain range detected by DIC, which may indicate weld failure. Weld failure would reduce effective load transfer to the specimen, producing an artificial strain drop and requiring test termination. Following testing, all test articles were examined using XCT to evaluate weld integrity. Selected post-test specimens underwent further characterization using advanced microscopy to provide detailed assessment of weldment microstructure and degradation mechanisms.

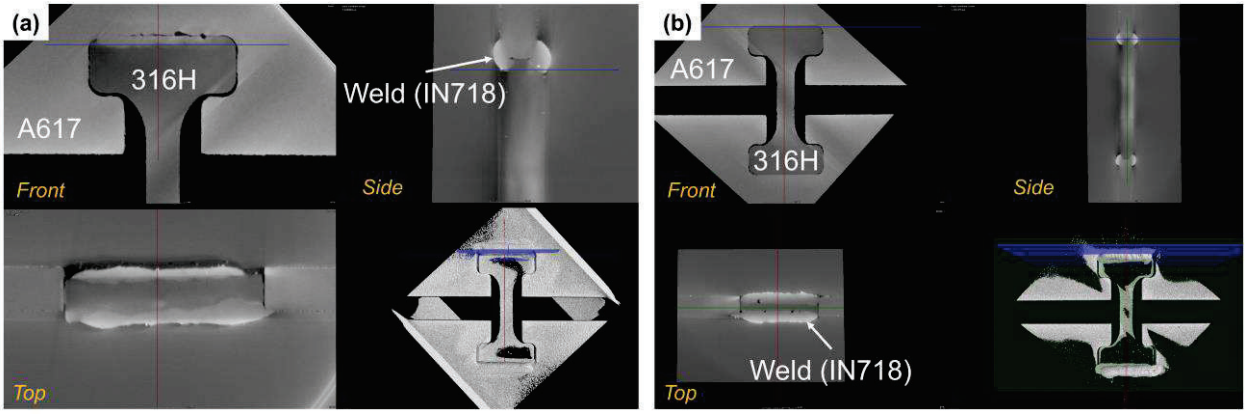

Figure 5. X-CT images of WSTA-S5 and WSTA-S6 before testing.

2.3. Surveillance Test Article Tests in Salt Bath

The eutectic NaCl–$MgCl_2$ mixture was prepared from high-purity NaCl and $MgCl_2$ salts (procured from Sigma Aldrich), while the FLiNaK eutectic salt was synthesized from LiF, NaF, and KF (procured from BeanTown Chemicals). All salt components were handled inside an argon-filled glovebox to prevent contamination from moisture and oxygen, as molten salt corrosion is highly sensitive to impurities. To further minimize the potential contaminants prior to eutectic mixture preparation, each salt component was purified by sequential baking in glassy carbon crucibles. The purification process involved stepwise heating to 120 °C, 180 °C, 250 °C, 350 °C, and finally 400 °C, with a minimum one-hour hold at each temperature. A calibrated muffle furnace with an accuracy of ±2 °C was used to heat salts at each target temperature. After baking, the salts were weighed and mixed in the appropriate proportions to achieve the eutectic compositions. A digital balance with an accuracy of 10-4 g was used to weigh the salt. Once salts became molten, FLiNaK salts were poured out into a glassy carbon or Ni boats to let them cool down to room temperature. However for NaCl-MgCl2 salt mixture, an additional chemical purification procedure was needed to further remove the possible dissolved impurities. 5 wt% Mg metal was added into the thermally purified salts and heated for 2 hours at 700°C. Mg metal reacts with oxygen and moisture to form MgO, precipitating on the bottom due to its extremely low solubility in salts. After this purification step, the extra Mg metal was removed from salts. The clear NaCl-MgCl2 salts on the top were carefully poured out and cooled down, while salts with precipitates on the bottom were disposed off. Thus, the eutectic salt mixtures prepared were broken into chucks, sealed in glass vials and stored in the glovebox for molten salt corrosion tests.

For molten salt exposure, the surveillance specimens were suspended vertically within the crucible using SS 316H support wires attached to a boron nitride (BN) lid. The wires were looped and wrapped at designated locations on the specimens such that they contacted only the SS 316H section while deliberately avoiding contact with the Alloy 617 frame. This arrangement minimized the risk of galvanic interactions or dissimilar metal corrosion that could otherwise influence the corrosion response of the alloys under investigation. The BN lid was selected for its chemical inertness and its stability at elevated temperatures. In addition, the use of BN eliminated the possibility of galvanic coupling effects that could arise from metallic holders, thereby ensuring that observed corrosion was attributable solely to salt–specimen interactions. The SS 316H wires provided sufficient mechanical strength to support the specimens during long-term thermal cycling. The entire test article, including both the central SS 316H specimen and the Alloy 617 drivers, was immersed in molten salt. Full immersion was necessary to maintain isothermal state of test article and evaluate the corrosion response of all material regions and alloy interfaces. To accommodate full immersion of the relatively large 2" × 2" specimen, a large glassy carbon crucible was used, requiring approximately 500 g of salt per batch to maintain complete coverage during the exposure. The crucible assembly used for specimen suspension and furnace test setup is shown in Figure 6.

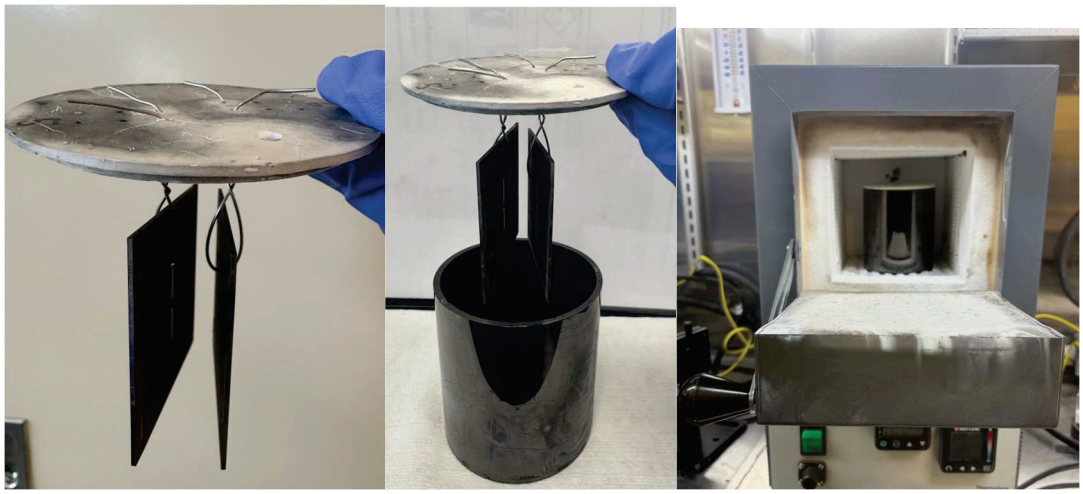

Figure 6. Specimen test setup for molten salt.

The 500 g salt batch was heated inside glassy carbon crucible under argon to 500°C, to achieve complete melting and homogenization prior to specimen exposure. Once the salts were molten and homogenized, the surveillance specimens were immersed and held for a total duration of 200 hr. The entire crucible assembly was then placed inside a high-temperature box furnace capable of cycling between 500 °C and 700 °C under an argon atmosphere, as illustrated in Figure 7.

During this period, the temperature was cycled between 500 °C and 700 °C to simulate thermal fluctuations representative of advanced reactor operating conditions. Each thermal cycle consisted of a 150-min heating ramp (from 500 °C to 700 °C), a 30-min isothermal soak at 700 °C, and a 180-min cooling phase (from 700 °C to 500 °C). Temperature was monitored using a dual thermocouple arrangement: one thermocouple was positioned directly inside the molten salt to record the melt temperature, while a second was located outside the crucible to monitor the furnace environment. This configuration ensured accurate temperature control and reliable monitoring of both local and bulk conditions. The thermal profile recorded over a period of 200 hr for FLiNaK and NaCl-MgCl2 is shown in Figure 7. For the test with FLiNaK, the thermocouple recording the furnace temperature noticed drop in measured values after about 50 hr (Figure 7a). This was due to movement of thermocouple during test. This did not affect the temperature cycling as salt temperature remained consistent throughout the test.

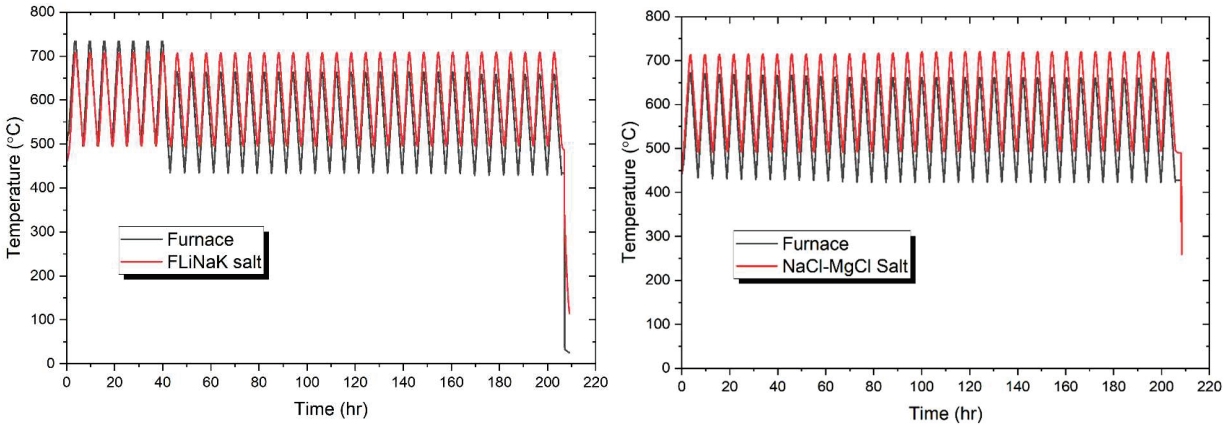

Figure 7. Thermal cycling profile for (a) FLiNaK, and (b) *NaCl-MgCl₂* test over a 200-hr exposure period showing temperature measurements from two thermocouples: one immersed in the molten salt and the other monitoring the furnace environment with heating ramp from 500°C to 700°C in 150 min, a 30-min soak at 700 °C, and a 180-min cooling phase.

2.4. Post-Test Evaluation

After thermal cycling the STA, the accumulated damage can be assessed through destructive or non-destructive techniques. This section presents two destructive techniques adopted to assess the accumulated damage in the SS 316H specimen.

2.4.1. Small Punch Test

Accumulated damage in the specimen can be further assessed through creep tests. However, the test article in reactor environment may experience irradiation which will led to activation of the test article. Conducting creep tests on the activated specimen using standard creep frames may not be feasible. The length of time required for performing a creep test is not conducive to analyzing the surveillance specimen during an outage or planned inspection. Also, the small size of the surveillance test specimen may cause difficulties when performing traditional uniaxial creep test. Thus, an alternate post-test evaluation process using the small punch test (SPT) is commonly used in the nuclear industry on structural materials, as only a small sample is required to study various mechanical properties and behaviors including tensile strength, creep, and fatigue, and various testing environments can be introduced to mimic corresponding conditions (Torres & Gordon, 2021). A small disk sample is often loaded by a semi-spherical punch or a ball, and a constant displacement or a constant load can be applied to obtain different properties (Arunkumar, 2020). Tensile and yield strengths can be obtained by applying a constant displacement to a specimen, and the test is commonly known as the SPT, while the small punch creep test (SPCT) allows for studying creep properties by applying a constant load at an elevated temperature for a prolonged period of time (Ganesh Kumar & Laha, 2015). This method is therefore an ideal approach to examine the post-test properties of the surveillance specimen. Most research chose a circular disk specimen with a diameter of 8 mm and thickness of 0.5 mm for a SPCT(Naveena & Komazaki, 2018), which is still too large to be extracted from the surveillance test specimen. Apart from the standard sample size, the CEN standard EN 10371:2021 suggests a miniature sample size with a diameter of 3 mm and thickness of 0.25 mm (compared in Table 1) (CEN, 2021). The smaller SPCT sample may be extracted after the surveillance test, if the flat surveillance specimen is changed to a circular tensile sample with a diameter of 3 mm. The analysis methods and new experimental setup are shown in this section, and the method will be validated to study the remaining creep life post surveillance test.

Table 1. Dimensions of the specimen and critical dimensions of apparatus for miniature and standard SPCT geometry (CEN, 2021).

Test Specimen	Specimen Diameter	Specimen Thickness	Holder Recess Diameter	Holder Recess Depth	Holder Receiving Hole Diameter	Holder Chamfer Length	Punch Diameter
Miniature	3.00	0.25	3.01	0.15	1.75	0.20	1.00
Standard	8.00	0.50	8.01	0.30	4.00	0.20	2.50

2.4.1.1. Theory

Apart from the dimension, the analytical methods of the SPT and SPCT can be challenging. Similar to a tensile test, a SPT produces a load F (N) and deflection u (mm) curve, and a SPCT is analyzed by a deflection u (mm) vs. time t (h) graph. However, as the SPT/SPCT is not a uniaxial testing method, the

test results cannot be directly interpreted as conventional tensile tests. The yield strength σ_y is often empirically correlated to the yield force F_y (N) (García et al., 2014; Isselin and Shoji, 2009):

$$\sigma_y = \beta_y \frac{F_y}{h_0^2} \quad (1)$$

where h_0 is the specimen thickness, and β_y is a correlation factor that is dependent on the initial thickness. Parameter $\beta_y = 0.510$ has been suggested for the standard sample size, and no correlation factor is provided for the miniature specimen (CEN, 2021).

The stress condition of a SPCT specimen is often studied by the Chakrabarty membrane stretch model (Chakraba.J, 1970; Torres & Gordon, 2021), and the equivalent uniaxial stress σ (MPa) can be obtained from the applied force F by using the Chakrabarty ratio Ψ:

$$\Psi = \frac{F}{\sigma} = 3.33\, k_{sp} r_r^{-0.2} r_p^{1.2} h_0 \ (N/MPa) \quad (2)$$

where r_r is the specimen holder recess radius, r_p is the punch radius, and k_{sp} is the correlation constant with an initial assumed value of 1. The ratios for the standard (ϕ 8 mm) and miniature (ϕ 3 mm) tests are $\Psi = 1.89$ N/MPa and $\Psi = 0.3686$ N/MPa respectively. They should only be used to choose the applied load from a desired stress value while planning the test (CEN, 2021), because these constant ratios are only dependent on the geometry (Dobes & Milicka, 2009). Based on an empirical analysis of a large data pool of SPCT (Holmström et al., 2018), the CEN standard (2021) recommends using the minimum deflection u_{min} of the specimen to convert the applied force F to the equivalent uniaxial stress σ:

$$\Psi = \frac{F}{\sigma} = 1.916\, u_{min}^{0.6579} \ (N/MPa) \quad (3)$$

The standard (CEN, 2021) also suggests obtaining the minimum strain rate $\dot{\varepsilon}_{min}$ from the minimum deflection rate $\dot{u}_{min}$:

$$\dot{\varepsilon}_{min} = 0.3922\, \dot{u}_{min}^{1.191} \ (1/h) \quad (4)$$

These equivalent factors allow for analysis of SPCT in the same way as conventional creep tests. However, this approach has only been validated on the standard (ϕ 8 mm) samples, as data pool size was not large enough for the miniature (ϕ 3 mm) specimen. Overall, there is a lack of reports in the literature on the miniature SPCT. In current research, the miniature SPCT will be compared with the standard test, and the analyzing method will be validated to allow for remaining creep life assessment of post surveillance test specimens.

2.4.1.2. Test apparatus

Both miniature and standard SPCT specimens are cut from a SS 316H sheet material according to the diameters listed in Table 1 and further ground and polished to the corresponding thickness with a final surface roughness of 0.25 μm. Post surveillance test SPCT specimens will be prepared in the same way as the miniature specimens.

A new experimental setup (Figure 8) has been designed to perform SPCT. A prepared specimen is held between the specimen holder and the upper die in the load chamber. To accommodate both the miniature and standard specimens, two die combinations are used (shown Figure 9) with the dimensions listed in Table 1. An alumina ball and a 18-8 stainless steel punch screw with the corresponding punch size are inserted into the hole of the upper die. The miniature and standard dies have the same outer diameter and height, and they are secured onto the stage bar by a threaded shell. The stage bar is attached to the lower stage, and an alumina rod is placed inside the hollow stage bar. A Keyence GT2 Linear Variable Differential Transformer (LVDT) sensor is installed in the lower stage, and it is connected to the

specimen via the ceramic rod to measure the deflection due to the high temperature in the load chamber. The lower stage and punch rod are attached to the load frame. An Instron 5848 Microtester universal testing machine and a load cell with a capacity of 2.0 kN have been selected due to the small size of the specimen. An ATS series 3210 three-zone split tube furnace (position shown in Figure 8) with a maximum temperature of 1100 °C is attached to the frame column. Four thermocouples are installed in the system: three in each zone of the furnace, and one is attached to the threaded shell to monitor the temperature of the specimen. Due to the high temperature of the test, all the components in the load chamber and the stage bar are made from Hastelloy X alloy, and other components are made from SS 316L. When a load is applied from the machine, the sample is deformed by the ceramic punch ball through the punch rod and the punch pin. The deflection of the specimen can be measured by the LVDT sensor through the ceramic bar.

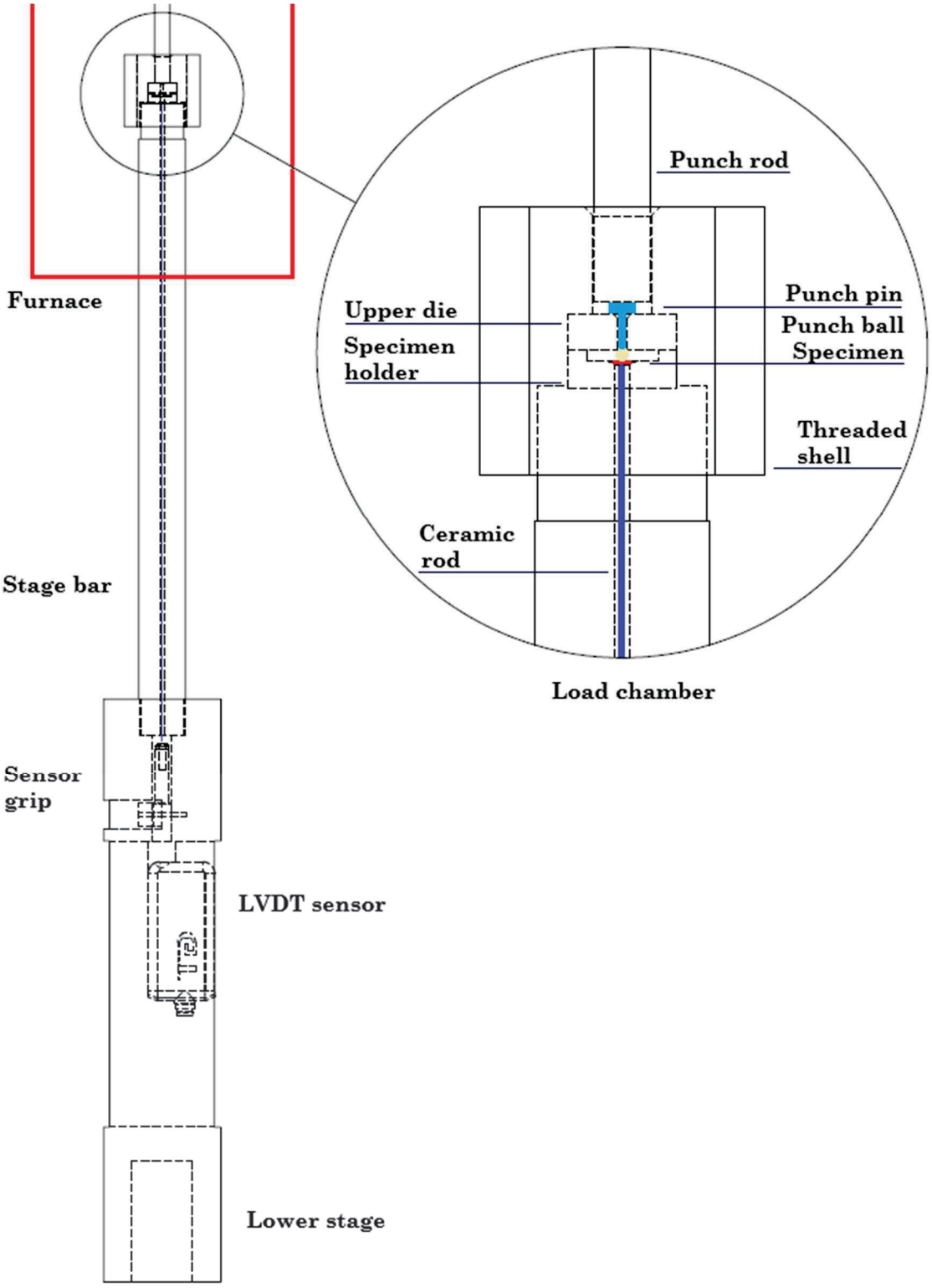

Figure 8. Schematic of the SPTC setup, where the location of the furnace is indicated by the red box, and components in the load chamber are shown in the detailed window.

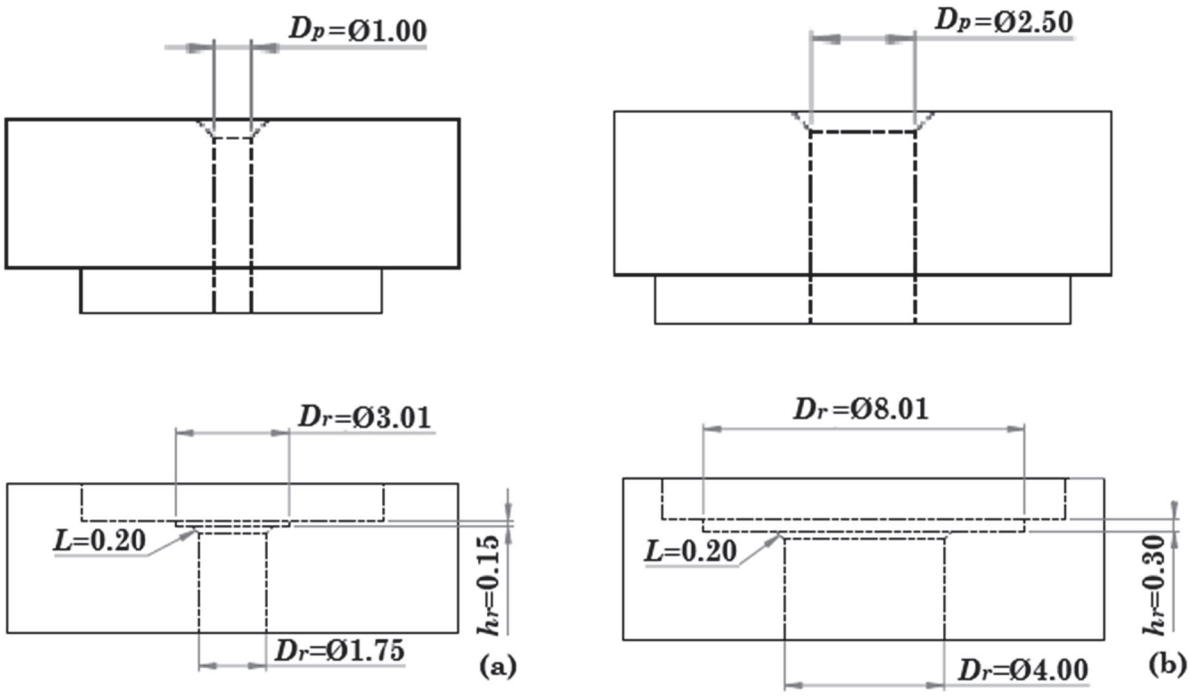

Figure 9. Drawings of the SPCT dies for different sample dimensions: (a) miniature samples (Ø 3.00 mm) and (b) standard samples (Ø 8.00 mm) (CEN, 2021).

2.4.2. Creep Rupture Test

Creep testing was conducted on a pristine SS 316H specimen as well as SS 316H specimens removed from a STA subjected to cyclic thermal testing in furnace air and molten salt environments. Figure 10a shows the creep testing setup, which consists of a three-dimensional DIC system to acquire strain data. For post-test specimens, samples were prepared using electric discharge machining to obtain the sample geometry shown in Figure 10b, where the gauge section consisted of SS 316H and the extended ends with two pin holes were Alloy 617 driver material. The pin holes were used for alignment while the specimen was gripped at the driver regions. Prior to testing, a high-temperature speckle pattern was applied. A dual-camera DIC system was used to capture full three-dimensional deformation. Creep testing was conducted on three specimens: cylindrical pristine SS 316H, WSTA-4 after testing in FLiNaK, and WSTA-6 after testing in NaCl-MgCl2. Creep testing was conducted at 700°C under a stress of 130 MPa. Post-creep fracture surfaces were examined using scanning electron microscopy (SEM). Additional salt-tested duplicates (WSTA-3 and WSTA-5) were analyzed using SEM to examine corrosion damage in the SS 316H gauge section, Alloy 617 driver materials, and welds. Energy dispersive spectroscopy (EDS) was further employed to map elemental distribution in regions affected by corrosion and across the weld interfaces.

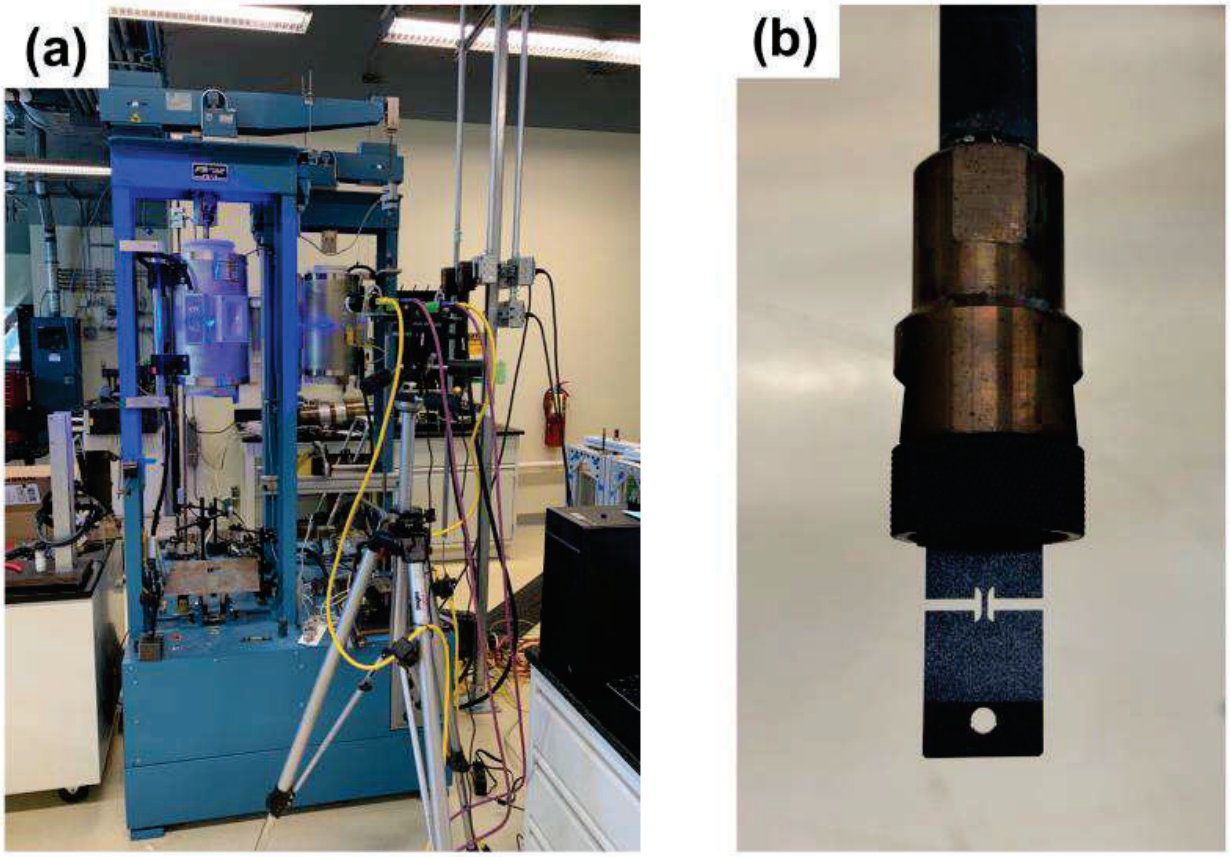

Figure 10. (a) Creep testing with DIC setup for testing pristine SS 316H and post-salt testing specimens. (b) Mounting of a specimen on the grips for creep testing.

3. EXPERIMENT RESULTS

3.1. Cyclic Thermal Testing in Air

A long-term test-to-rupture test was conducted on WSTA-1. Figure 11a, and Figure 11b show the overall temperature profile and strain evolution measured at the specimen gauge (Fig. 6a) and at the driver edges (Figure 11b). Figure 11c and Figure 12 further show the temperature and strain profiles at selected time intervals to reveal detailed response of strain with the increase of thermal cycles. The strain was calculated using the image taken at room temperature (before testing) as the strain-free reference. It can be observed from Figure 11a, and Figure 11c that the strain range gradually increased with the increase of thermal cycles in the beginning 150 h. The increase of strain range was due to cyclic strain hardening under creep-fatigue testing. Beyond this period, the strain range stabilized at ~0.77% (Figure 12a). The constant strain range continued until ~333 hr where a slight reduction of strain range occurred (Figure 12b). However, this strain range reduction was likely an artifact caused by unintended specimen disturbance relative to the DIC camera, as the same event was noticed from the strain profiles at the driver edges (Figure 11b). As the testing continued, a sudden drop of strain range in the specimen gauge section was observed at ~477 hr where the strain range dropped from 0.73% to 0.53%, as shown in Figure 12c. The reduced strain range remained constant for the remaining of the test until the testing was terminated at 525 hr. Figure 11b shows that the strain range across the edges of the Alloy 617 drivers was constant after ~150 hr and till the end of the experiment. The constant strain range across the drivers and sudden drop of strain at the specimen gauge section indicated potential failure of the welds between the

specimen and drivers. When cracks formed in the welds during creep-fatigue, the load from the drivers cannot be effectively transferred to the specimen, leading to a reduced strain range in the gauge but a constant strain range across the drivers. Figure 11b shows that a gradual increase of strain range across the edge of drivers was observed in the beginning of the testing, which is consistent with the strain response from the specimen gauge. This matching strain response indicated that the weldments were effective in the beginning but failed after repeated creep-fatigue cycles. This phenomenon was also observed in FY24 during test-to-rupture cyclic testing of a WSTA which was welded using SS 316 as the filler material. XCT scans of the WSTAs with SS 316 filler material showed defects in the welds, which propagated during testing and reduced in strain range reduction. In FY25, Inconel 718 was used as the filler material to provide better weld strength. XCT scans (Figure 5) of all WSTAs showed crack-free welding prior to testing. However, these weldments did not survive the repeated cyclic creep-fatigue loading.

The post-test WSTA-a was examined using optical microscopy and SEM. Figure 13a shows optical micrographs of the two welds between the specimen and drivers. No visible defects were observed under optical microscopy. Optical measurements at areas between edge of drivers and columns (Figure 13b) indicated out-of-plane bending of the drivers relatively to the columns. Similar out-of-plane bending was observed previously due to compressive residual stress in the specimen after testing

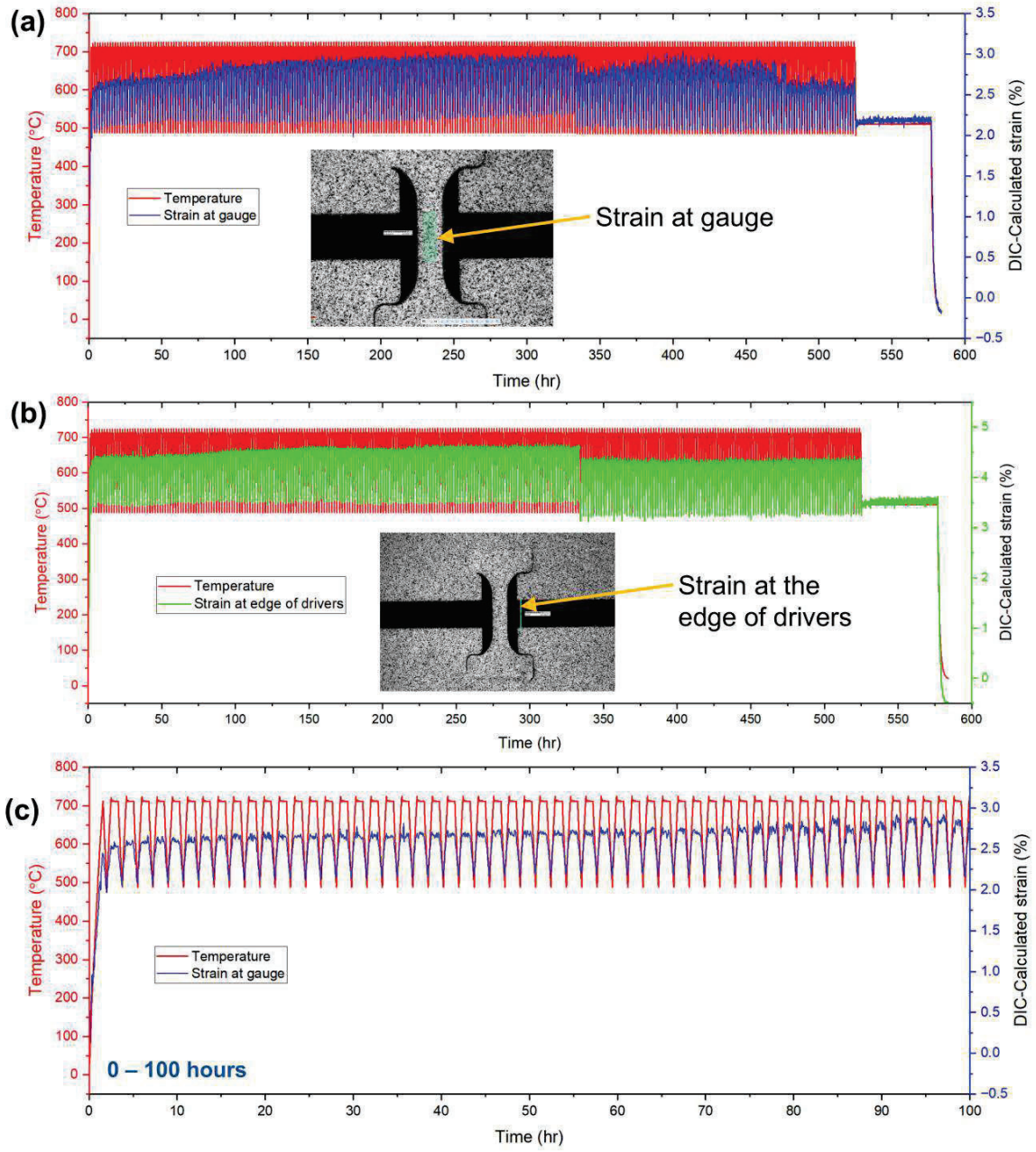

Figure 11. Temperature and strain profiles from the (a) specimen gauge section and (b) edge of Alloy 617 drivers during test-to-rupture testing of WSTA-1 in air. (c) Temperature and strain profiles for the first 100 hr showing gradual increase of strain range with the increase of testing cycles.

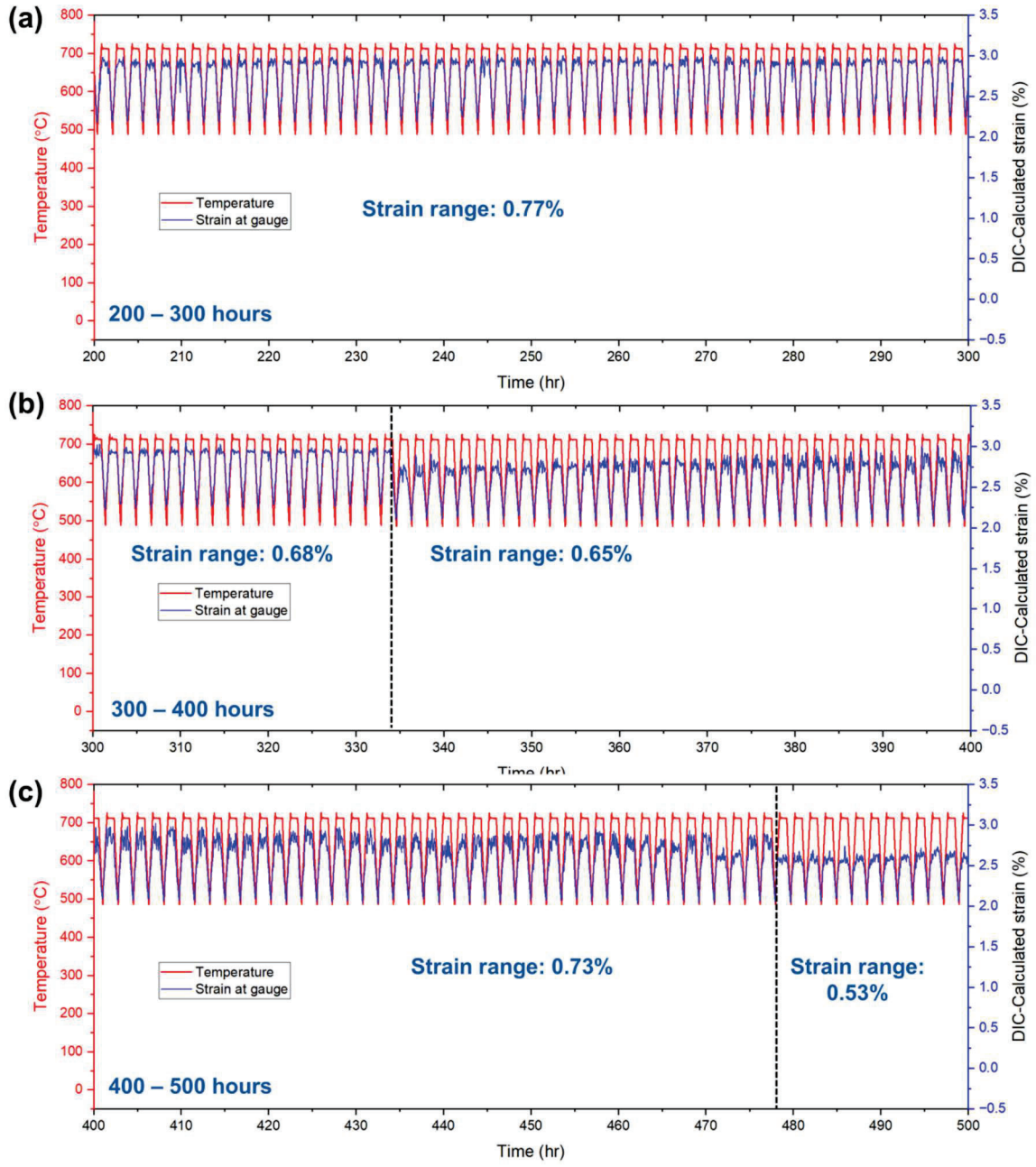

Figure 12. Temperature and strain profiles for (a) 200 – 300 hr, (b) 300 – 400 hr, and (c) 400 – 500 hr from test-to-rupture testing of WSTA-1 in air. A constant strain range of 0.77% was observed during 200 – 300 hr while the strain range reduced to 0.53% at ~477 hr.

Figure 13c-e shows the microstructure at the driver-specimen joint of post-test WSTA-1. As shown in Figure 13c, the joint consisted of three regions: the SS 316H specimen, the Inconel 718 weld, and the Alloy 617 driver. The specimen and driver materials exhibited equiaxed grains typical of wrought plates, while the welds contained elongated grains. A cellular sub-grain structure was observed within the welds (Figure 13e). Cracks were identified at the joint, primarily within the Inconel 718 weld region. These cracks initiated and propagated along the grain boundaries (Figure 13e). These cracks were likely attributed to residual stress generated during welding, compounded by repeated stress and deformation from creep-fatigue testing. These cracks resulted in the reduced strain range from the testing (Figure 12c).

Figure 13f shows the micrograph at the specimen gauge and Figure 13g shows the distribution of major elements in this region. A thin Cr- and Ni-rich oxide layer was detected on the gauge surface, formed due to oxidation at elevated temperatures. Although microstructural defects were observed at the gauge, these defects did not cause rupture of the specimen during testing.

Maintaining defect-free welds is essential to ensure effective transfer of the creep-fatigue loading to the specimen. To improve weld quality, a double-bevel design was adopted to increase welding penetration depth, and welding parameters were further optimized. Multiple dissimilar-metal welds between Alloy 617 and SS 316H were fabricated to validate the revised procedure. As shown in Figure 14, the optimized process achieved ~90% penetration across the specimen thickness, with microstructural examination confirming defect-free bonding. These optimized welding geometries and parameters were subsequently applied to fabricate two additional STAs. At the time of this report, one of these test articles had undergone 500 hr cyclic thermal testing in air.

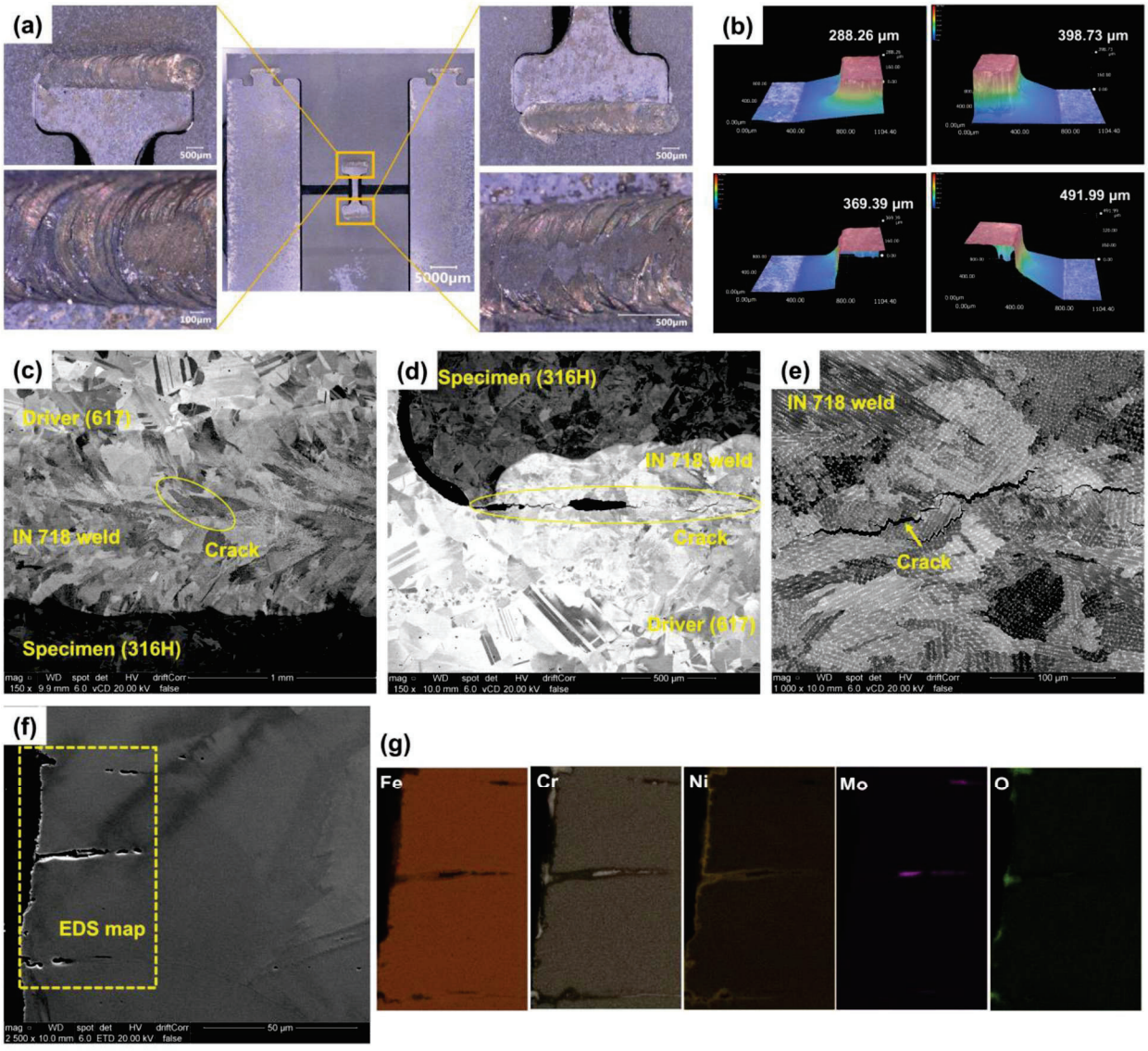

Figure 13. Optical micrographs of the post-test WSTA-1 showing the (a) welds and (b) out-of-plane bending. (c-d) SEM micrographs showing the microstructure at the joints at various locations where cracks were observed. (f) SEM image and (g) elemental distribution at the specimen gauge.

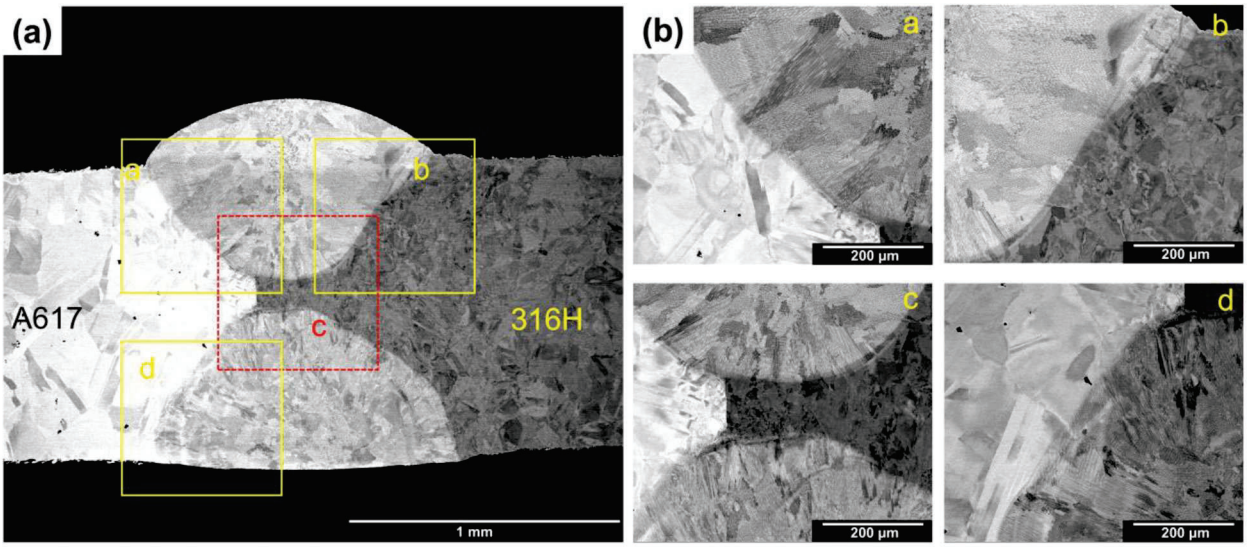

Figure 14. SEM micrographs showing an (a) overview and (b) detailed microstructure of a weldment with double-bevel design at SS 316H and improved welding parameters.

3.2. Cyclic Thermal Testing in Molten Salt

The WSTAs tested in molten salts were examined using XCT to identify cracks or defects in the welds and gauge regions. Figure 15 shows XCT images of test articles after exposure in NaCl-MgCl2 (Figure 15b and Figure 15c) and FLiNaK (Figure 15d and Figure 15e), as well as the WSTA-2 (Figure 15a) tested in argon as a reference. The XCT analysis revealed crack formation near the welds following molten salt exposure. For the test articles in NaCl-MgCl2 (WSTA 3 and 4), cracks were observed at the SS 316H section near the welds (Figure 15b and Figure 15c). These cracks were oriented primarily perpendicular to the welds. The XCT resolution (~8 µm) did not reveal visible defects at the specimen gauge. In contrast, FLiNaK-tested specimens exhibited a different cracking morphology, with more extensive cracking in the Alloy 617 drivers adjacent to the specimen (Figure 15d and Figure 15e). These cracks can even be observed from the surface of the test articles under optical microscopy (Figure 15f). Cracks in the specimens were not observed. To further investigate crack morphology, WSTA-3 and WSTA-5 were sectioned, mounted, and polished following standard sample preparation procedures for SEM analysis.

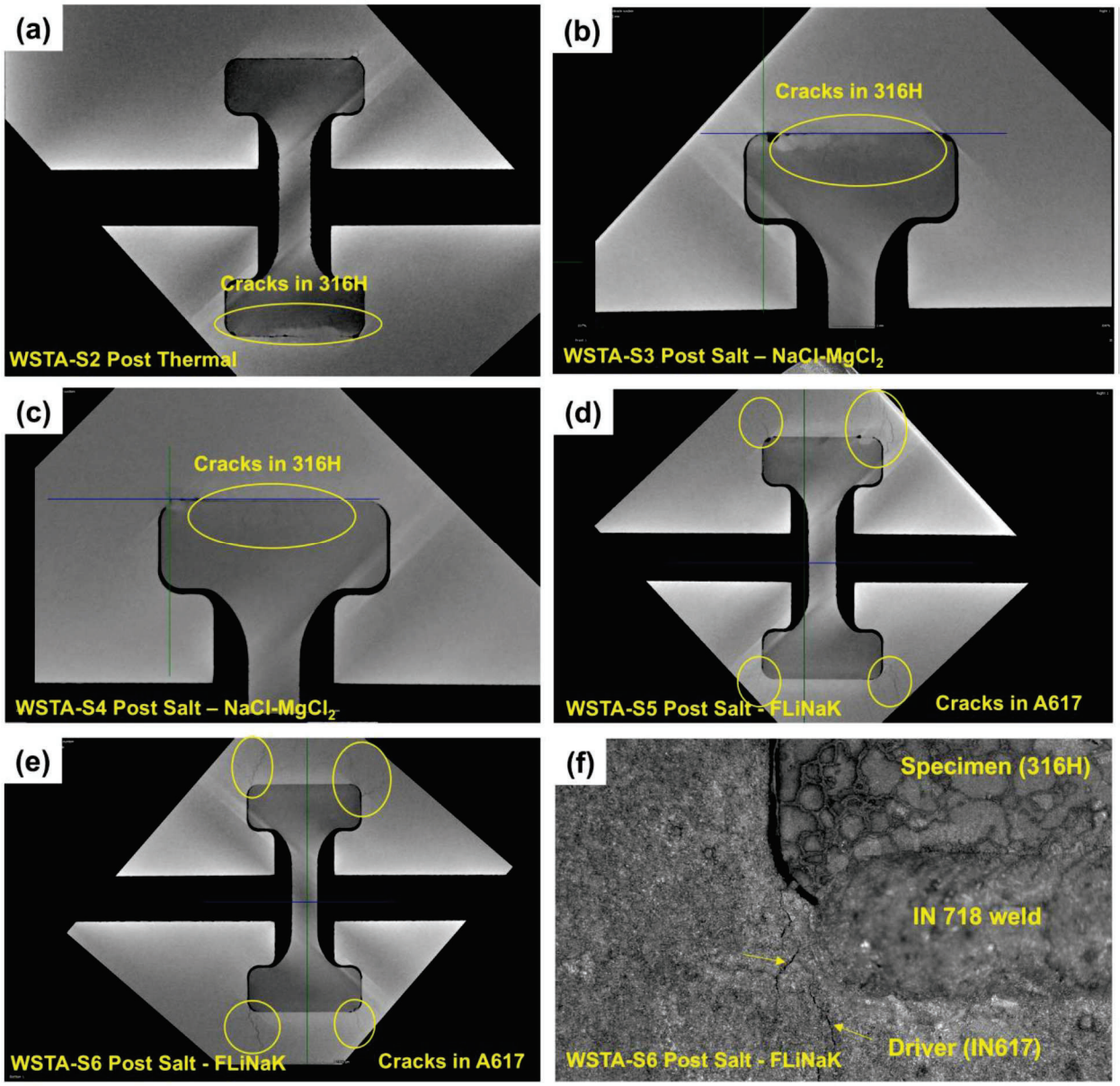

Figure 15. XCT images of the WSTAs after testing in (c, d) NaCl-MgCl2 and (e, f) FLiNaK salts and the reference WSTAs after identical thermal exposure (no salt) from molten salt testing.

Figure 16 shows the microstructure at the upper joint (Figure 16 a) and lower joint (Figure 16b) between specimen and weld, as well as an overview of the upper joint (Figure 16c). Multiple cracks were observed in the SS 316H specimen near the welds, consistent with XCT scans. The cracks were at grain boundaries. Additionally, a pore was observed in the weld due to trapped gas during welding. To understand the origin of cracking, EDS mapping was conducted in a region containing cracks, as shown in Figure 17. The EDS maps revealed depletion of Cr along cracks, which indicates selective dissolution of Cr into the salt as a driver for void formation and intergranular crack propagation. Residual stress from the welding process may also promote stress corrosion cracking. Residual stress can accelerate the diffusion of Cr at grain boundaries, creating corrosions that promote intergranular cracking. Salt composition was not detected.

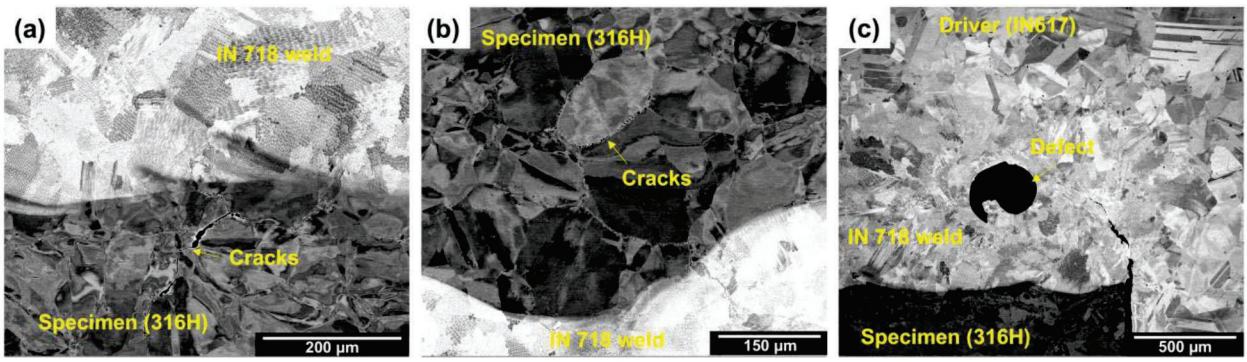

Figure 16. Microstructure at the welds of WSTA-3 after testing in NaCl-MgCl2.

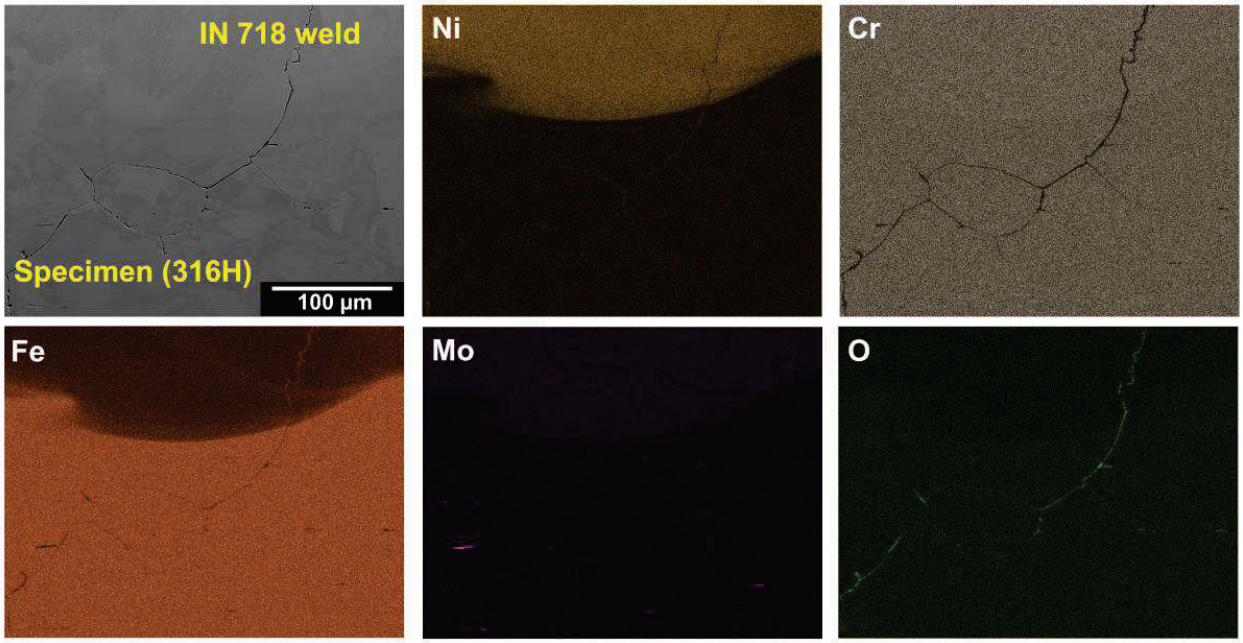

Figure 17. Microstructure and elemental distribution at the welds near SS 316H specimen of WSTA-3.

Corrosion attacks at the specimen gauge were revealed as shown in Figure 18. Depletion of Cr can be observed from EDS maps (Figure 18c). Measurements were conducted along the peripheries of the gauge section to evaluate salt attack depth. An average attack depth of 23.6 ± 15.8 mm and a maximum attack depth of 86.6 µm were measured. Therefore, cyclic thermal testing of the test articles in NaCl-MgCl2 created defects in the SS 316H gauge. Corrosion in A617 driver was also examined. Cr depletion was observed at grain boundaries as marked in Figure 19. The corrosion attack depth was about 30 µm. Additionally, the layer on the A617 surface could be caused by the deposition of corrosion projects from the SS 316H specimen and columns since the Alloy 617 has minimal Fe content (max 3 wt.%).

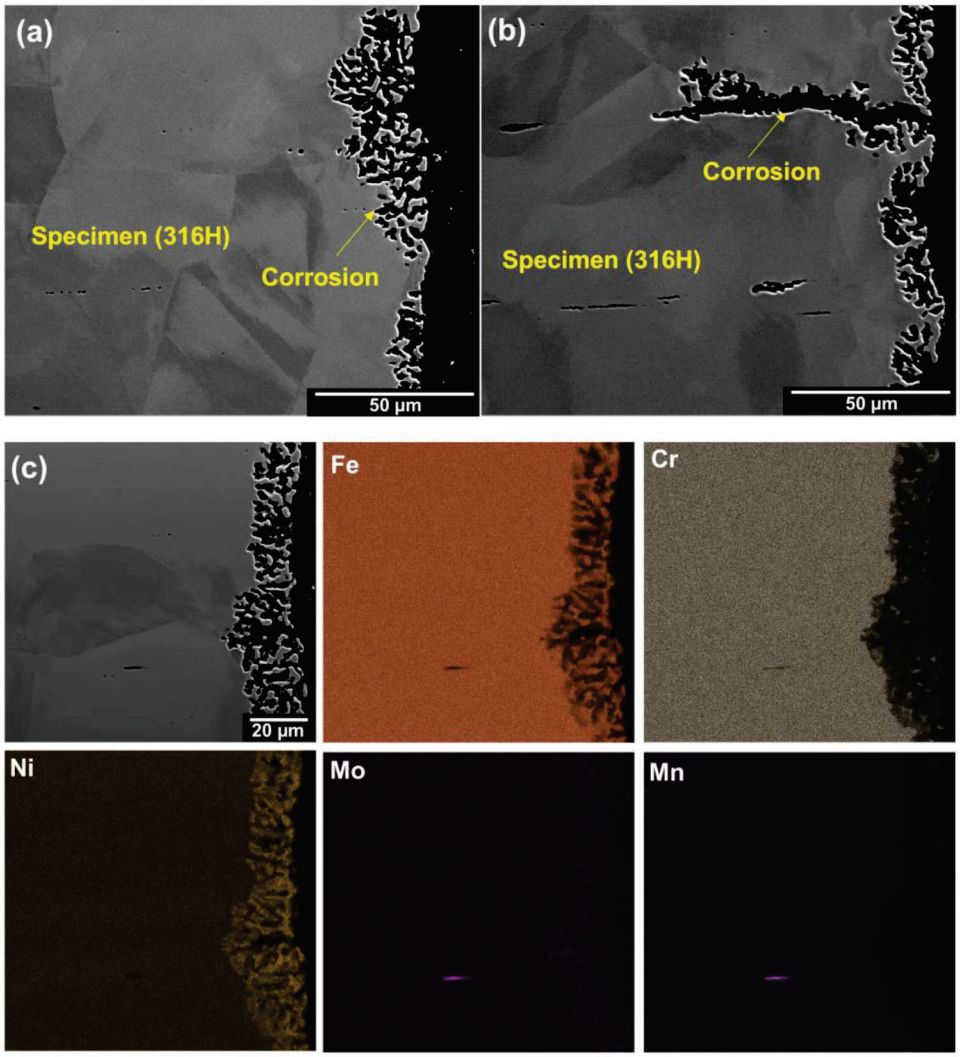

Figure 18. (a-b) Microstructure and (c) elemental distribution at the SS 316H gauge of WSTA-3.

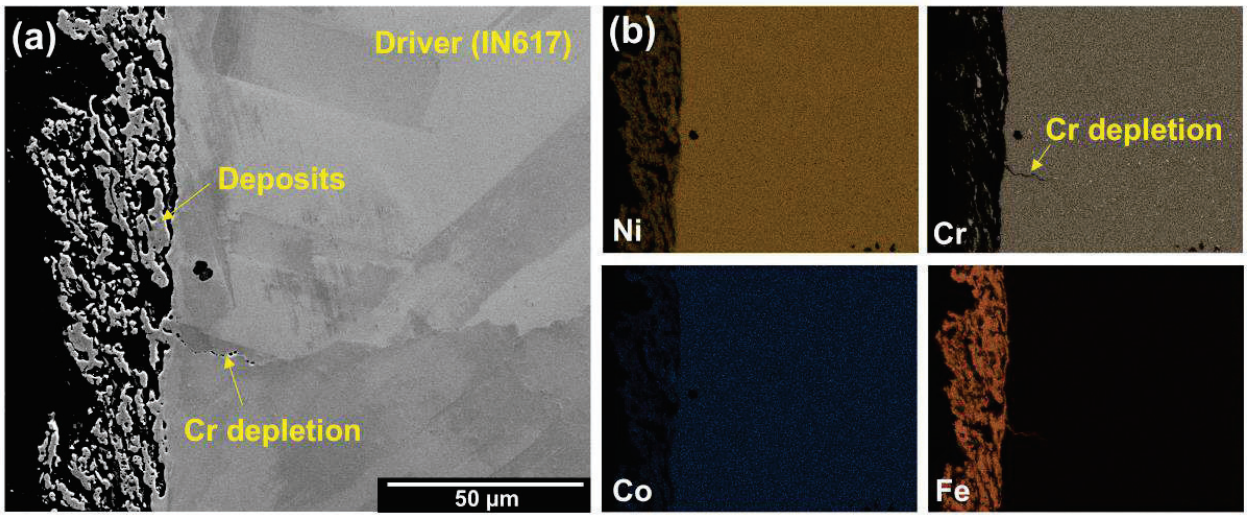

Figure 19. (a) Microstructure and (b) elemental distribution at the edge of A617 driver.

Figure 20 shows the microstructure of WSTA-5 near the joints after testing in FLiNaK salt. Cracks were observed in the test article after salt exposure, and these cracks were mostly distributed in the Alloy 617 driver near the welds. The location of these cracks is consistent with the XCT scans as shown in Figure 20d-f. These cracks propagated along the Alloy 617 grain boundaries. Elemental distribution near these cracks was revealed by EDS. The EDS maps (Figure 21) show depletion of Cr in the grain boundaries as marked by the red arrow. Selective depletion of Cr along grain boundaries caused cracking as marked by the yellow arrow in Figure 21a. Therefore, it is suspected that the cracking in Alloy 617 driver near welds was induced by the combination of salt penetration and welding-induced residual stress.

Characterization of the microstructure at specimen gauge shown in Figure 22b revealed cracks due to salt attack, as confirmed by EDS maps (Figure 22c). Measurements of salt attack depths were conducted at >20 spots and the average attack depth is 35.8 µm. The maximum attack depth was measured to be 132.5 µm. This figure also shows that 200 hr thermal cyclic testing in FLiNaK salts resulted in more damage in the SS 316H gauge compared to the testing in NaCl-MgCl2 salts. Additionally, FLiNaK induced more cracking in the test articles compared to NaCl-MgCl2.

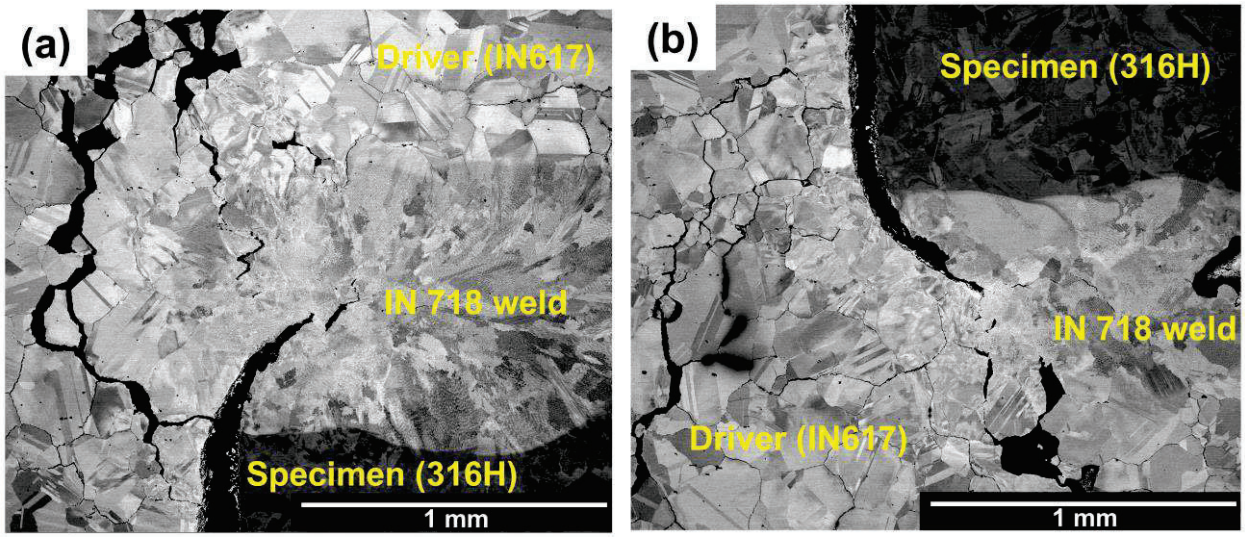

Figure 20. Microstructure at the (a, b) upper and (c) lower joints in WSTA-5 showing presence of intergranular cracking at the Alloy 617 drivers near the welds.

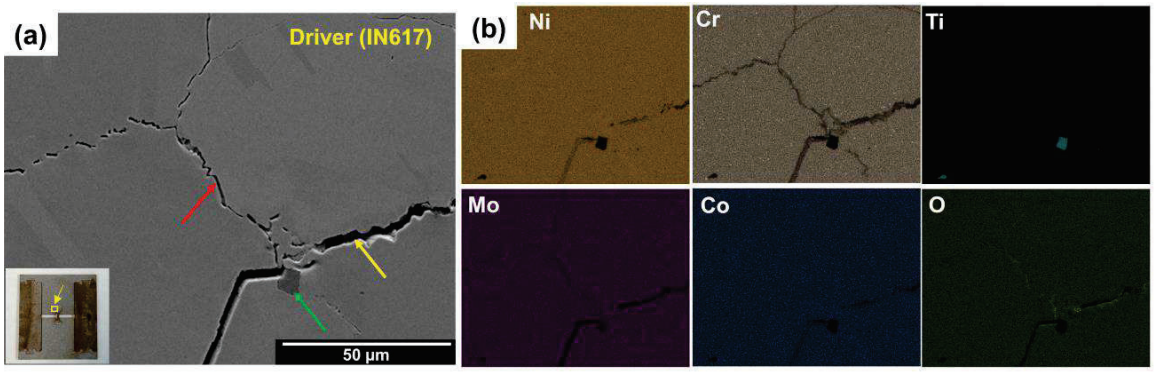

Figure 21. Distribution of major elements near cracks in Alloy 617 driver near the welds and specimen.

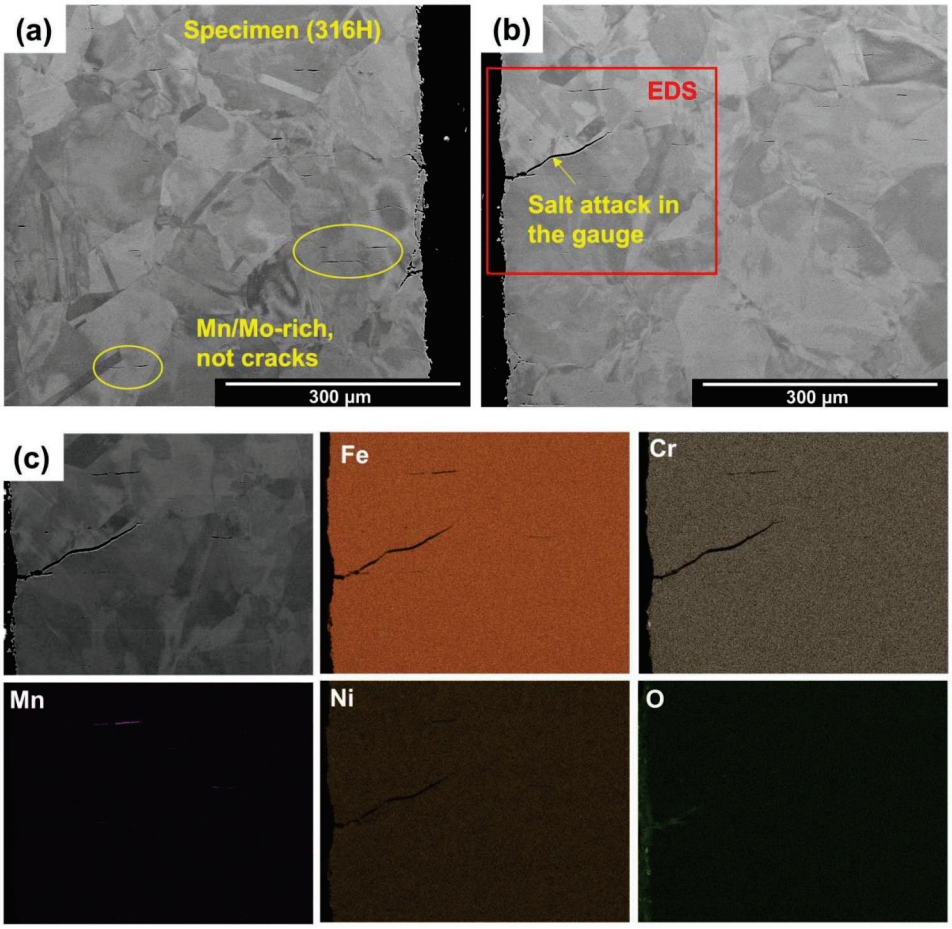

Figure 22. (a) Microstructure and (b) EDS maps of SS 316H at the gauge of WSTA-5 showing the corrosion damage.

The Alloy 617 driver at the edge of the test article away from the SS 316H specimen (marked in Figure 23a) was examined. The microstructure (Figure 23a) and EDS maps (Figure 23b) clearly revel Cr-depletion at the grain boundaries. Corrosion attack depth was significant, showing >200 µm corrosion damage. Corrosion in Alloy 617 driver as revealed in Figure 20, Figure 21, and Figure 22 may indicate that concern of using Alloy 617 as the driver material since the driver material was expected to have minimal corrosion compared to the specimen (SS 316H in this case). Corrosion in drivers can cause degradation of the driver material, which affect the creep strength and intended design of the test article. Therefore, this project also evaluated Alloy 244 as the driver material in FY25. A revised test article design as shown in Figure 4b was finalized to adopt Alloy 244 as the driver material. Alloy 244 as the driver material can provide several benefits. First, Alloy 244 has much less Cr content (8 wt.%) compared to Alloy 617 (20 to 24% of Cr). Therefore, Cr depletion-induced cracking is expected to be mitigated in Alloy 244. Moreover, Alloy 244 does not have cobalt in its composition whereas Alloy 617 has 10 to 15 wt.% of cobalt. The cobalt in Alloy 617 limited the location where the test article can be placed to eliminate the formation of cobalt-60. In addition, Alloy 244 has a lower coefficient of thermal expansion (CTE, 8.9 × 10-6/°C) compared to Alloy 617 (11.6× 10-6/°C). The larger mismatch of CTE between Alloy 244 and SS 316H enables the further shrinkage of the size of test articles to apply same stress as Alloy 617, or increase of the stress with the same test article geometry. Welding of Alloy 244 to SS 316H is currently being analyzed using XCT to ensure the quality of welds before furnace and molten salt testing.

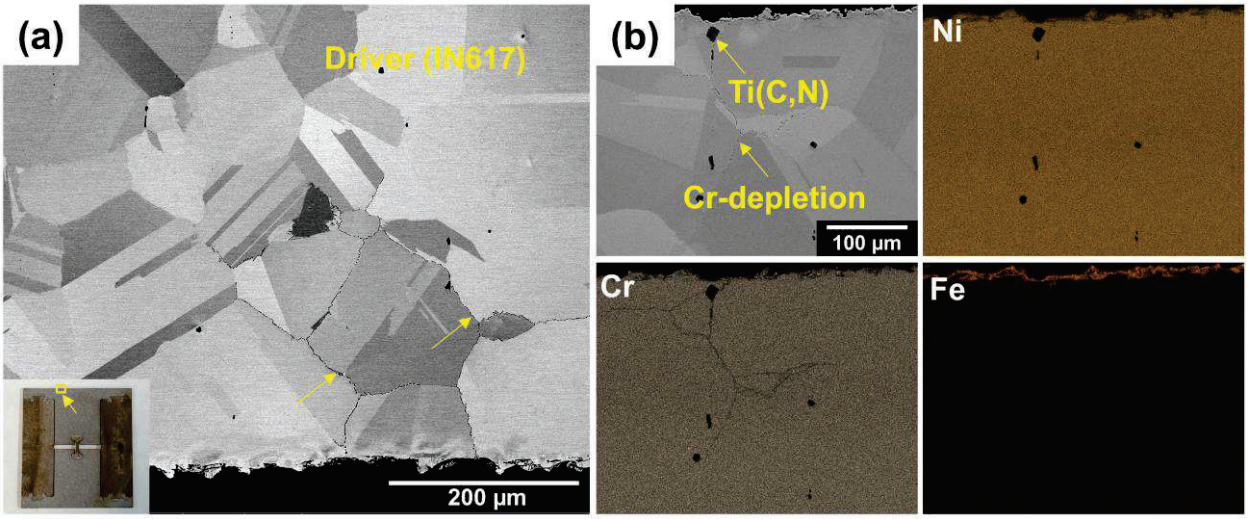

Figure 23. (a) Microstructure and (b) elemental distribution in A617 driver at the edge of test article away from the SS 316H specimen as indicated in the inserted image in (a).

Following the 200-hr thermal cycling test, visible condensation of salt vapors was observed on the outer surface of the crucible and along the interior walls of the furnace (see Figure 24). Although NaCl–$MgCl_2$ salt is generally stable up to 700 °C, it begins to vaporize at temperatures exceeding this threshold. To maintain a target temperature of 700 °C during the soak phase, the furnace setpoint had to be slightly elevated, resulting in peak salt temperatures reaching approximately 713 °C during each cycle. This marginal overshoot led to incremental vaporization of the salt with each cycle. Post-test inspection revealed a noticeable reduction in salt level, indicating that the specimens—initially fully submerged—experienced a gradual change in immersion depth over time. As a result, weight loss measurements from this test may not reliably reflect uniform exposure conditions across all cycles. Given the thermal instability of the NaCl–$MgCl_2$ system under these conditions, future exposure tests will instead focus on the more stable FLiNaK salt.

Figure 24. Condensation of salt vapors observed on the outer surface of the crucible and along the interior walls of the furnace following thermal cycling. These deposits are indicative of partial vaporization of NaCl–$MgCl_2$ salt during repeated exposures to peak temperatures slightly exceeding 700°C

3.3. Creep Testing

Figure 25 shows the creep curves of a pristine SS 316H and specimens after testing in molten salt. The pristine SS 316H had a creep-rupture life of 891 hr while the specimen after testing in NaCl-MgCl2 and FLiNaK had a reduced creep-rupture life of 293 hr and 76 hr, respectively. The creep strain follows a similar trend. The creep strain of pristine SS 316H was 29.4% while the test articles after testing in NaCl-MgCl2 and FLiNaK had a creep strain of 6.0% and 2.4%, respectively. Post-salt creep testing shows the specimens after salt exposure had a significant decrease in creep rupture life and creep strain compared to the wrought material. Therefore, accumulation of damage was evidenced in the test articles during molten salt environment and cyclic thermal loadings. The post-test creep experiments demonstrated the method to estimate material remaining life for material degradation analysis. Figure 26 shows the morphologies of fracture surfaces in the longitudinal section. The result shows that the cracks initiated in the corrosion attacked region and propagated along grain boundaries under creep loading. The corrosion attack depth in SS 316H specimen after exposure in FLiNaK was larger compared to that in the specimen after testing in NaCl-MgCl2, which caused shorter rupture life and strain of the WSTA-6 compared to WSTA-3.

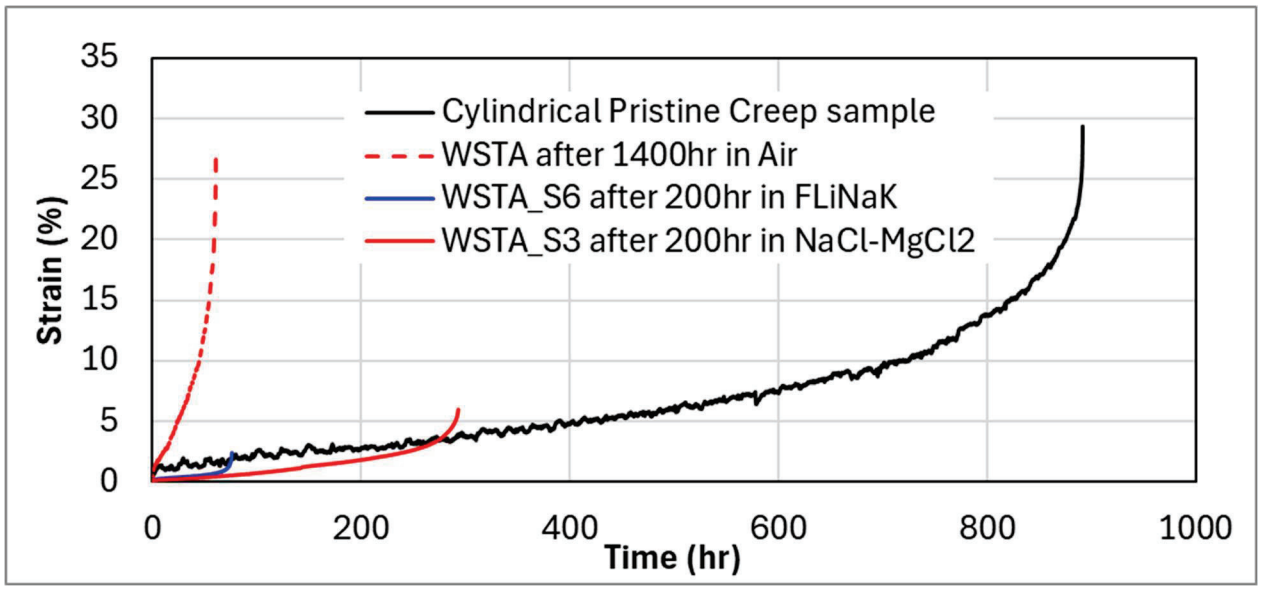

Figure 25. Creep curves tested at 700°C and 130 MPa of pristine SS 316H, SS 316H specimens after 1400 hr of cyclic testing in air, and SS 316H specimens after 200 hr cyclic thermal testing in FLiNaK and NaCl-MgCl2 salts.

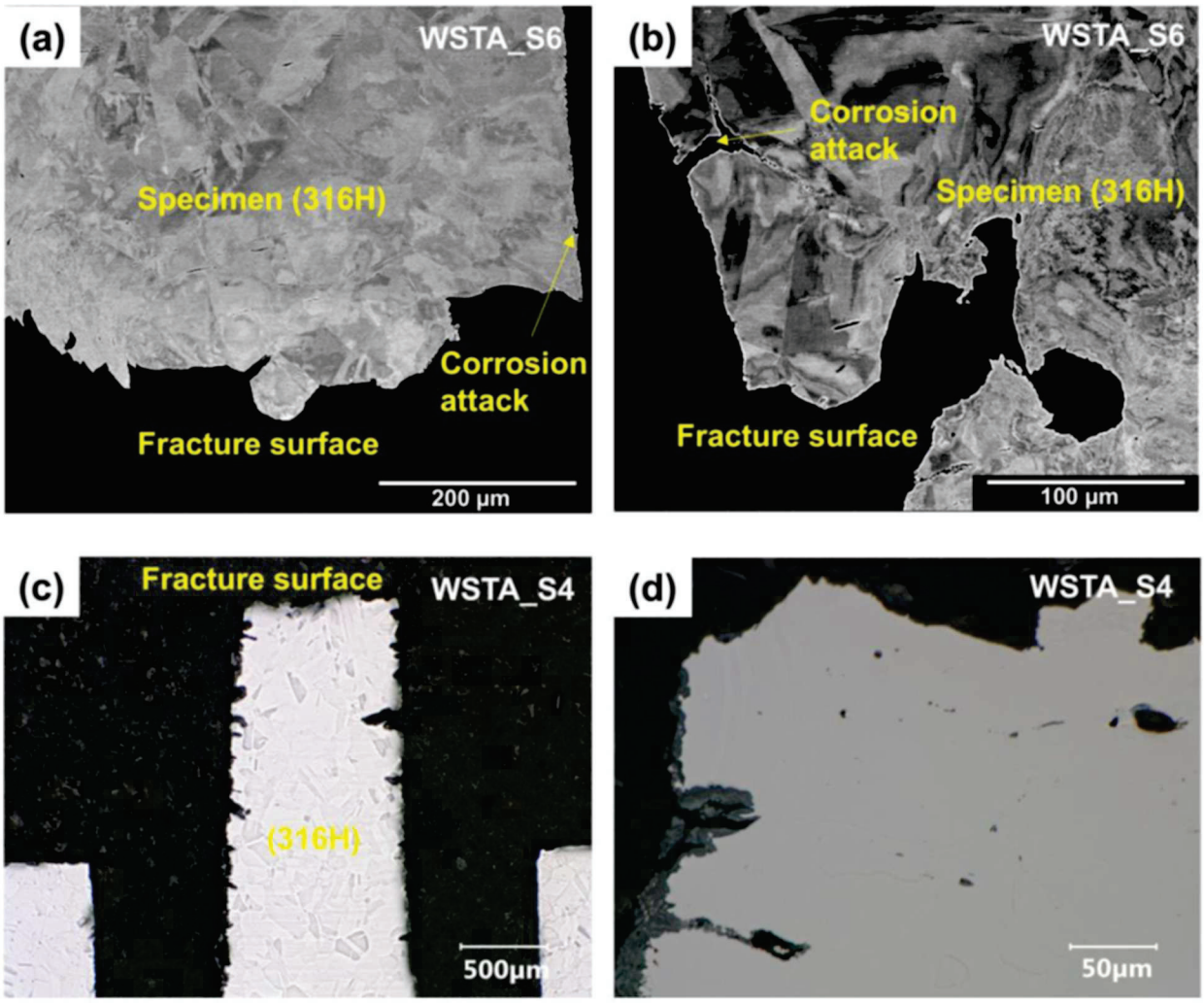

Figure 26. Fracture morphologies of test articles after testing in (a, b) FLiNaK and (c, d) NaCl-MgCl2 salts.

4. EVALUATION OF POST-TEST MEASUREMENTS

The total damage experienced by the surveillance test article is defined as the linear summation of mechanical damage and damage due to corrosion. The creep test data conducted on the surveillance specimen so far, was used to assess the remaining life of specimen using the damage assessment per ASME Section III Division 5 HBB (ASME, 2025). Note that ASME evaluates only mechanical damage of specimen, and any premature failure represents influence due to corrosion damage.

For the STAs that were tested in salt environment, the strain history information was not recorded. Thus, a constant total strain range of 0.75% was assumed during thermal cycles of test articles. The mechanical strain range is calculated as 0.33% by subtracting the thermal strain range from the total strain range, and the cycles to failure for SS 316H available in ASME Section III Division 5 Table HBB-II-4000-2. ASME implements a factor of 2&20 in the development of number of cycles to failure for fatigue life. Thus, the cycles to failure calculated from Table HBB-II-4000-2 were multiplied by factor 20 to calculate the average cycles to failure. The average cycles to failure is used to calculate fatigue damage fraction.

For creep damage, stress history is calculated using the mechanical strain history measured from the DIC. A standalone model with a viscoplastic constitutive model discussed in nonmandatory appendix HBB-Z is used. An isothermal maximum temperature of 700°C is assumed for the entire time in the model, and mechanical strain history is applied as a uniaxial load. The calculated stress history is used to determine the incremental creep damage. For specimens tested in salt environment, stress history is assumed based on the salt temperature cycle and viscoplastic constitutive model discussed in nonmandatory appendix HBB-Z is used. The stress history obtained from simulations was used to calculate the creep damage fraction. The detailed calculation results are presented in Table 2.

Table 2. Damage calculation on STA tested in air, FLiNaK, and NaCl-MgCl2

Load Cycle	Calculation Steps	Environment		
		Air	FLiNaK	NaCl-MgCl2
Temperature cycling in environment	Applied number of cycles	350	33	33
	Average cycles to failure (20xNf)	19760	19760	19760
	Fatigue damage fraction	0.0177	0.0017	0.0017
	Creep damage fraction	0.4211	0.0396	0.0396
Remaining life	Remaining creep damage assessment	0.5387	0.9565	0.9565
	Remaining creep life (hr)	480	852	852
Pure creep test	Rupture time at end of pure creep test	61	76	293

For test article tested in air environment, the strain range reduction was observed around 350th cycle and reached nearly zero mechanical strain range. Hence, damage fractions are calculated up to the 350th cycle. For articles in salt environment, test was discontinued after 200 hr of thermal cycles, which indicates total of 33 cycles of thermal cycles. For salt environment tests, mechanical strain range is assumed to be same as strain rage of specimen tested in air. Hence, the average cycles to failure is same for all tests. Fatigue and creep damage fractions are calculated for applied thermal profiles. The remaining life is assed by the difference of calculated damage fractions and the nearest intersection of damage envelope for a given fatigue damage fraction, shown schematically in Figure 27. The remaining creep life is calculated by multiplying the remaining creep damage fraction by the time to rupture on the pristine ASTM circular sample (891 hr). The anticipated creep lives are compared against the observed time to rupture and presented in Table 2.

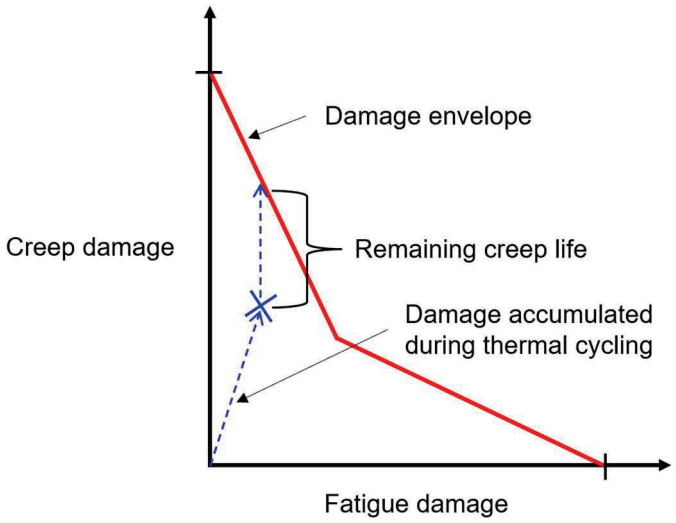

Figure 27. Schematic representation of remaining creep life assessment based on damage envelope.

Note that these creep tests were performed on the miniature creep test specimen. Due to small size, ensuring uniaxial load the test specimen in the standard creep frame was difficult. The test specimen, that experienced temperature cycles in air, underwent small torsion along with slight offset loading which led to additional bending loads. Thus, the creep life of miniature creep specimen with air environment has shown a significant lower rupture life compared to anticipated rupture life. Thus, new grippers that minimize the torsion on the specimen and improve uniaxial loads were adopted. These tests will be repeated on new samples, to determine the remaining lives for different environments and assess the accumulated damage through the damage envelope using ASME Section III Division 5 creep-fatigue assessment.

These calculations show the applicability of the STAs. The test articles will be placed in the reactor with known temperature profile. During the secluded inspection, the test article will be removed from the reactor and evaluated through either destructive or non-destructive techniques. This report presents the destructive technique. The post-exposure creep life is compared against the anticipated creep life determined from the mechanical loads calculated based on the known temperature history of test articles. This information provides the damage accumulated due to corrosion and irradiation as the difference between anticipated and measured life. This gives damage information of component material, which then could be used to assess remaining life of component.

5. SUMMARY

This report presents the ongoing work on STA development and presents experimental methods to evaluate the working principles of material surveillance technology. Test articles were tested in air, FLiNaK, and NaCl-MgCl2. Initial evaluation led to critical improvements such as weld procedure development to improve the load transfer mechanisms between specimen-driver and driver-column interface. The localized damage near welded region in drivers showed the importance of interlocking test article geometry. The remaining life assessment in the post-test evaluation would assist the development of the acceptance criteria for test articles. The calculation procedure in the post-test measurements shows the applicability of STAs.

Planned work for FY2026 includes:

1. Interlocking test article: Develop an interlocking test article for cylindrical test specimen and minimize with standard machining tolerance to minimize gaps between specimen-driver and driver-column interface.

2. Thermal cycling in Molten Salt: Continue thermal cycling of STA in molten salt environment and assess the material damage after post-exposure.

3. Small punch test: Conduct SPCT on cylindrical disk specimens to develop creep rates to aid the acceptance criteria development for material surveillance technology

4. Driver material selection: Explore refractory metals as driver materials to reduce the test article size and conduct thermal testing in salt environments.

6. REFERENCES

Arunkumar, S. (2020). Overview of Small Punch Test. Metals and Materials International, 26(6), 719-738. https://doi.org/10.1007/s12540-019-00454-5

ASME International. 2025. "Section III, Rules for Construction of Nuclear Facility Components, Division 5, High Temperature Reactors." in ASME Boiler and Pressure Vessel Code: An International Code. New York, NY.

ASTM International Standards E531-23. "Standard Practice for Surveillance Testing of High-Temperature Nuclear Component Materials." American Society for Testing and Materials.

CEN. (2021). EN 10371:2021 Metallic materials - Small punch test method. In: The National Standards Authority of Ireland.

Chakraba.J. (1970). A Theory of Stretch Forming over Hemispherical Punch Heads. International Journal of Mechanical Sciences, 12(4), 315-&. https://doi.org/Doi 10.1016/0020-7403(70)90085-8

Dobes, F., & Milicka, K. (2009). Application of creep small punch testing in assessment of creep lifetime. Materials Science and Engineering a-Structural Materials Properties Microstructure and Processing, 510-11, 440-443. https://doi.org/10.1016/j.msea.2008.04.087

Ganesh Kumar, J., & Laha, K. (2015). Small Punch Creep deformation and rupture behavior of 316L(N) stainless steel. Materials Science and Engineering: A, 641, 315-322. https://doi.org/10.1016/j.msea.2015.06.053

García, T. E., Rodríguez, C., Belzunce, F. J., & Suárez, C. (2014). Estimation of the mechanical properties of metallic materials by means of the small punch test. Journal of Alloys and Compounds, 582, 708-717. https://doi.org/10.1016/j.jallcom.2013.08.009

Holmström, S., Li, Y., Dymacek, P., Vacchieri, E., Jeffs, S. P., Lancaster, R. J., Omacht, D., Kubon, Z., Anelli, E., Rantala, J., Tonti, A., Komazaki, S., Naveena, Bruchhausen, M., Hurst, R. C., Hähner, P., Richardson, M., & Andres, D. (2018). Creep strength and minimum strain rate estimation from Small Punch Creep tests. Materials Science and Engineering a-Structural Materials Properties Microstructure and Processing, 731, 161-172. https://doi.org/10.1016/j.msea.2018.06.005

Isselin, J., & Shoji, T. (2009). Yield Strength Evaluation by Small-Punch Test. Journal of Testing and Evaluation, 37(6), 531-537. <Go to ISI>://WOS:000272486300003

M. C. Messner et al., "Assessment of Passively Actuated In-Situ Cyclic Surveillance Test Specimens for Advanced Non-Light Water Reactors," in Proc. ASME Pressure Vessels and Piping Conference, July 15–20, 2018, (Vol. 51593, p. V01BT01A018). Available: https://doi.org/10.1115/PVP2018-84793.

M. C. Messner and T.-L Sham. "Preliminary Procedures and Acceptance Criteria for in-situ Structural Materials Surveillance for MSR," ANL-ART-229, Argonne National Laboratory, Lemont, IL, September 2021. https://www.osti.gov/biblio/1817876.

Mahajan, Heramb Prakash, Xinchang Zhang, Kaelee Novich, Michael D. McMurtrey, Tate Patterson, Ting-Leung Sham, and Mahmut Nedim Cinbiz. Development of surveillance test articles with reduced dimensions and material volumes to support msr materials degradation management. No. INL/RPT-23-74540-Rev000. Idaho National Laboratory (INL), Idaho Falls, ID (United States), 2023.

McMurtrey, M. D., et al. 2022. "Phase II Development of the Surveillance Test Articles to Improve the Design, Fabrication, and Testing." INL/RPT-22-69281, Idaho National Laboratory, Idaho Falls, ID. https://www.osti.gov/biblio/1906467

Naveena, & Komazaki, S.-i. (2018). Effect of specimen size on small punch creep behavior of high nitrogen ferritic heat-resistant steels. Materials Science and Engineering: A, 721, 311-318. https://doi.org/10.1016/j.msea.2018.02.030

Nuclear Engineering Material model Library, https://neml.readthedocs.io/en/dev/index.html (accessed Aug. 1, 2023). (NEML)

Torres, J., & Gordon, A. P. (2021). Mechanics of the small punch test: a review and qualification of additive manufacturing materials. Journal of Materials Science, 56(18), 10707-10744. https://doi.org/10.1007/s10853-021-05929-8

Zhang, Xinchang, Heramb Prakash Mahajan, and Michael D. McMurtrey. Design, Fabrication and Testing of Surveillance Test Articles for MSR Materials Degradation Management. No. INL/RPT-24-80975-Rev000. Idaho National Laboratory (INL), Idaho Falls, ID (United States), 2024.